3D oupling approa h between dis rete and ontinuum models for dynami simulations (DEM-CNEM)

Mohamed Jebahi, Jean-Luc Charles, Frédéric Dau, Lounes Illoul, Ivan Iordanoff

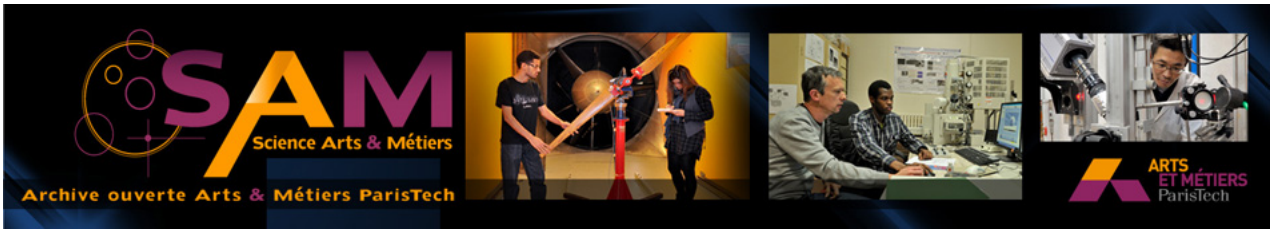

3D coupling approach between discrete and continuum models for dynamic simulations (DEM-CNEM)

Mohamed JEBAHI[a], Jean-luc CHARLES[b], Frederic DAU[b], Lounes ILLOUL[c], Ivan IORDANOFF[b]

[a] *Univ. Bordeaux, I2M, UMR 5295, F-33400 Talence, France*
[b] *Arts et Metiers ParisTech, I2M, UMR 5295 CNRS F-33400, Talence, France*
[c] *Arts et Metiers ParisTech, 151, Boulevard de l'Hôpital, F-75013 Paris, France*

Abstract

The coupling between two dissimilar numerical methods presents a major challenge, especially in case of discrete-continuum coupling. The Arlequin approach provides a flexible framework and presents several advantages in comparison to alternative approaches. Many studies have analyzed, in statics, the ingredients of this approach in 1D configurations under several particular conditions. The present study extends the Arlequin parameter studies to incorporate a dynamic behavior using 3D models. Based on these studies, a new 3D coupling method adapted for dynamic simulations is developed. This method couples two 3D codes: DEM-based code and CNEM-based code. The 3D coupling method was applied to several reference dynamics tests. Good results are obtained using this method, compared with the analytical and numerical results of both DEM and CNEM.

Keywords: multiscale method, coupling method, discrete element, natural element, Arlequin approach, dynamic simulation

1. Introduction

The discrete element method (DEM) [1, 2] presents an alternative way to study physical phenomena requiring a very small scale analysis or those which cannot be easily treated by continuum mechanics, such as wear, fracture and abrasion problems. In the past decades, an increasing interest in the discrete element method has led to the development of many interesting variations of this method. The most recent variation involves modeling the interaction between particles by cohesive beams [1]. This method correctly simulates the 3D linear elastic behavior of the continua. However, numerical simulations are very time consuming (CPU-wise). Furthermore, a very great number of particles are required to discretize small domains. This method does not consider large structure simulations. However, in most situations, the effects that must be captured by DEM are localized in a small portion of the studied domain. Thus, the use of a specific multiscale method to treat the phenomena at each scale appears to be advantageous. A challenge that arises in the multiscale coupling approach is that the high frequency portion of waves are often spuriously reflected at the small/coarse scale interface. This phenomenon has already been addressed using the finite element model with different element sizes [3].

The importance of this multiscale approach has attracted many researchers. Therefore, several papers have been published on the subject, and many coupling methods have been developed. These methods can be divided in two classes: edge to edge methods and methods with overlapping zones (called overlap methods). The first class [4, 5] is mainly applied to static studies. Indeed, using this method, it is very difficult to reduce spurious reflections at the interface between models. Therefore, this class will not be treated in this paper. The second class seems to be more applicable to dynamic studies, which is the scope of the present work.

Ben Dhia [6, 7, 8], in a pioneer work, developed the Arlequin approach as a general framework that allows the intermixing of various mechanical models for structural analysis and computation.

Abraham et al. [9, 10] developed a methodology that couples the tight-bending quantum mechanics with the molecular dynamics such that the two Hamiltonians are averaged in an overlapping zone. A damping was used in the overlapping zone to reduce the spurious reflections at the interface between the two models. Nevertheless, the choice of the damping coefficient remains difficult.

Smirnova et al. [11] developed a combined molecular dynamics (MD) and finite element method (FEM) model with a transition zone in which the FEM nodes coincide with the positions of the particles in the MD region. The particles in the transition zone interact via the interaction potential with the MD region. At the same time, they experience the nodal forces due to the FEM grid.

Belytschko and Xiao [4, 12] have developed a coupling method for molecular dynamics and continuum mechanics models based on a bridging domain method. In this method, the two models are overlaid at the interface and constrained with a Lagrange multiplier model in the overlapping subdomain.

Jacob et al. [13] formulated an atomistic-continuum coupling method based on a blend of the continuum stress and the atomistic force. In term of equations, this method is very similar to the Arlequin method.

In an interesting work, Chamoin et al. [14] have analyzed the main spurious effects in the atomic-to-continuum coupling approaches and they proposed a corrective method based on the computation and injection of dead forces in the Arlequin formulation to offset these effects.

Aubertin et al. [15] applied the Arlequin approach to couple the extended finite element method XFEM with the molecular dynamics MD to study dynamic crack propagation.

Bauman et al. [16] developed a 3D multiscale method, based on the Arlequin approach, between highly heterogeneous particle models and nonlinear elastic continuum models.

Recently, Combescure et al. [17] formulated a 3D coupling method, applied for fast transient simulations, between the smoothed particle hydrodynamics SPH and the finite element method. This coupling method is, also, based on the Arlequin approach.

For more details, a review of these methods can be found in [18]. A common feature of overlap coupling methods is that a weight function is introduced to partition a certain quantity in the overlapping zone. Herein, the Arlequin approach [6, 7, 19] is used to develop a 3D multiscale method adapted for dynamic simulations between the constrained natural element method (CNEM) and the discrete element method (DEM). The DEM version, which is used in this work, is the most recent version developed by André [1]. The CNEM is a mesh-free method, but it is very close to the finite element method. The coupling method developed here can avoid spurious wave reflections without any additional filtering or damping. Indeed, the fine scale solution is projected onto the coarse scale solution in the overlapping zone at each time step. Thus, it filters the high frequencies coming from the fine scale model (discrete model), which are greater than the cutoff frequency of the coarse scale model (continuum model). This paper is organized as follows: in Section 2, the governing equations of both the DEM and CNEM models are given. Subsequently, we describe how both models are coupled using the Arlequin approach in the most general case. In Section 3, several interesting previous studies on the Arlequin parameter are summarized: including mathematical studies of Ben Dhia et al. [7, 20], the studies of Bauman et al. [21] and the static 1D numerical studies of Guidault et al. [22]. After, the different Arlequin parameters are studied dynamically using 3D models. In Section 4, this new coupling method is validated for tensile-compression, bending and torsional loadings on beams. Section 5 presents the conclusions and outlooks.

2. The problem statements

A domain Ω is considered with boundary $\partial\Omega = \partial\Omega^u + \partial\Omega^T$ such that displacements and tractions are prescribed on $\partial\Omega^u$ and $\partial\Omega^T$, respectively. This domain is divided into two subdomains, Ω_C and Ω_d, which are modeled using the continuum approach and the discrete approach, respectively. An isotropic linear elastic behavior and small deformation gradients are assumed for simplicity. The governing equations of both the continuum and the discrete subdomains are recalled in Subsections 2.1 and 2.2, while ignoring the coupling conditions. These conditions will be introduced after detailing the coupling approach in Subsection 2.3.

2.1. Continuum subdomain Ω_C

As an isolated system, the governing equations in the continuum subdomain Ω_C can be written as: $\forall\ \boldsymbol{x} \in \Omega_C(t)$ and $t \in [0,T]$, given the initial conditions, find $(\boldsymbol{u}, \boldsymbol{\sigma}) \in [\mathcal{H}^1(\Omega_C)]^3 \times [\mathcal{L}^2(\Omega_C)]^6$ such that:

$$\left\{\begin{array}{lcll} div(\boldsymbol{\sigma}) + \rho \boldsymbol{f} & = & \rho \ddot{\boldsymbol{u}} & \text{in} \quad \Omega_C \\ \boldsymbol{\sigma} & = & \boldsymbol{A} : \boldsymbol{\varepsilon}(\boldsymbol{u}) & \\ \boldsymbol{\varepsilon}(\boldsymbol{u}) & = & \frac{1}{2}(\nabla \boldsymbol{u} + \nabla^t \boldsymbol{u}) & \\ \boldsymbol{u} & = & \boldsymbol{u}_d & \text{on} \quad \partial\Omega_C^u \\ \boldsymbol{\sigma}.\boldsymbol{n} & = & \boldsymbol{T}_d & \text{on} \quad \partial\Omega_C^T \end{array}\right. \tag{1}$$

where ρ is the density, $\boldsymbol{u}$ is the continuum displacement vector, $\boldsymbol{\sigma}$ is the Cauchy stress tensor, $\boldsymbol{\varepsilon}$ is the strain tensor, $\boldsymbol{A}$ is the stiffness tensor, $\boldsymbol{f}$ is the body force vector, $\boldsymbol{u}_d$ defines the prescribed displacement vector on $\partial\Omega_C^u$ and $\boldsymbol{T}_d$ is the prescribed traction vector on $\partial\Omega_C^T$.
The associated weak formulation can be written as: find $\boldsymbol{u} \in \mathcal{U}^{ad}$ such that, given the initial conditions, $\forall\ \delta\boldsymbol{u} \in \mathcal{U}^{ad,0}$:

$$\int_{\partial\Omega_C^T} \delta\dot{\boldsymbol{u}} \cdot \boldsymbol{T}_d \, d\Gamma - \int_{\Omega_C} \boldsymbol{\varepsilon}(\delta\dot{\boldsymbol{u}}) : \boldsymbol{A} : \boldsymbol{\varepsilon}(\boldsymbol{u}) \, d\Omega + \int_{\Omega_C} \rho \ \delta\dot{\boldsymbol{u}} \cdot \boldsymbol{f} \, d\Omega = \int_{\Omega_C} \rho \ \delta\dot{\boldsymbol{u}} \cdot \ddot{\boldsymbol{u}} \, d\Omega \tag{2}$$

with $\delta\dot{\boldsymbol{u}}$ as a test function and the admissible solution spaces, $\mathcal{U}^{ad}$ and $\mathcal{U}^{ad,0}$, are defined as follows:
$\mathcal{U}^{ad} = \left\{\boldsymbol{u} = \boldsymbol{u}(\boldsymbol{x},t) \in [\mathcal{H}^1(\Omega_C)]^3; \boldsymbol{u} = \boldsymbol{u}_d \text{ on } \partial\Omega_C^u; \forall\ t \in [0,T]\right\}$
$\mathcal{U}^{ad,0} = \left\{\boldsymbol{u} = \boldsymbol{u}(\boldsymbol{x},t) \in [\mathcal{H}^1(\Omega_C)]^3; \boldsymbol{u} = \boldsymbol{0} \text{ on } \partial\Omega_C^u; \forall\ t \in [0,T]\right\}$

2.2. Discrete subdomain Ω_d

In an isolated system of the discrete domain Ω_d which is a set of spherical particles that interact via cohesive beams, the governing equations can be written as: for $i = 1..n_p$ and $t \in [0,T]$, given the initial conditions, find $(\boldsymbol{d}_i, \boldsymbol{\theta}_i, \boldsymbol{f}_{/i}^{int}, \boldsymbol{c}_{/i}^{int}) \in \mathbb{R}^3 \times \mathbb{R}^3 \times \mathbb{R}^3 \times \mathbb{R}^3$ such that:

$$\left\{\begin{array}{lcl} \boldsymbol{f}_{/i}^{ext} + \boldsymbol{f}_{/i}^{int} & = & m_i \ddot{\boldsymbol{d}}_i \\ \boldsymbol{c}_{/i}^{ext} + \boldsymbol{c}_{/i}^{int} & = & I_i \ddot{\boldsymbol{\theta}}_i \end{array}\right. \tag{3}$$

with $\boldsymbol{d}_i$, $\boldsymbol{\theta}_i$, m_i and I_i representing the displacement vector, the rotation vector, the mass and the mass moment of inertia of the i^{th} particle, respectively. $\boldsymbol{f}_{/i}^{ext}$ and $\boldsymbol{c}_{/i}^{ext}$ represent the total external forces and the total external torques applied on the i^{th} particle, respectively. $\boldsymbol{f}_{/i}^{int}$ and $\boldsymbol{c}_{/i}^{int}$ are the total internal forces and the total internal torques applied by other particles via the cohesive beams on the i^{th} particle, respectively.

$$\left\{\begin{array}{lcl} \boldsymbol{f}_i^{int} & = & \displaystyle\sum_{j=0}^{nnp} \boldsymbol{f}_{ij} = \sum_{j=0}^{nnp} (E_\mu S_\mu \frac{\Delta l_\mu}{l_\mu} \boldsymbol{x} - \frac{6E_\mu I_\mu}{l_\mu^2}((\theta_{jz} + \theta_{iz})\boldsymbol{y} + (\theta_{jy} + \theta_{iy})\boldsymbol{z})) \\ \boldsymbol{c}_i^{int} & = & \displaystyle\sum_{j=0}^{nnp} \boldsymbol{c}_{ij} = \sum_{j=0}^{nnp} (\frac{G_\mu I_{O\mu}}{l_\mu}(\theta_{jx} - \theta_{ix})\boldsymbol{x} - \frac{2E_\mu I_\mu}{l_\mu^2}((\theta_{jy} + 2\,\theta_{iy})\boldsymbol{y} + (\theta_{jz} + 2\,\theta_{iz})\boldsymbol{z})) \end{array}\right. \tag{4}$$

With:

- nnp is total number of neighbor particles of the i^{th} particle
- $\boldsymbol{f}_{ij}$ and $\boldsymbol{c}_{ij}$ are beam reaction forces and torques acting on the i^{th} particle by the j^{th} one, respectively.
- $(O_i, \boldsymbol{x}, \boldsymbol{y}, \boldsymbol{z})$ is local frame associated to the beam connecting i^{th} and j^{th} particles.
- $\boldsymbol{\theta}_i(\theta_{ix}, \theta_{iy}, \theta_{iz})$ and $\boldsymbol{\theta}_j(\theta_{jx}, \theta_{jy}, \theta_{jz})$ are the rotations of beam cross sections expressed in the beam local frame.

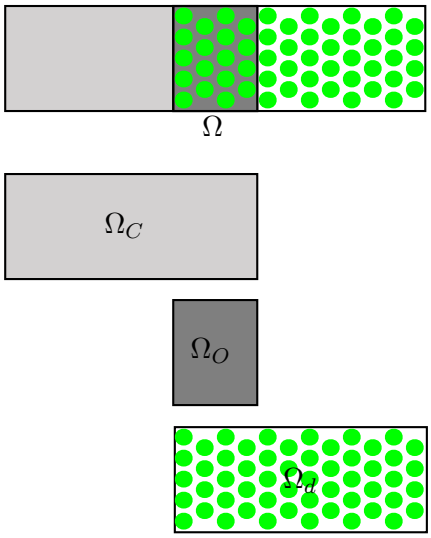

Figure 1: Global domain decomposition

- l_μ, S_μ, $I_{O\mu}$ and I_μ are the beam length, beam cross section area, polar moment of inertia and moment of inertia along $\boldsymbol{y}$ and $\boldsymbol{z}$.
- E_μ and $G\mu$ are the beam Young and shear modulus.

As in the continuum, the associated weak formulation can be defined as follows: find $(\boldsymbol{d}, \boldsymbol{\theta}, \boldsymbol{f}, \boldsymbol{c}) \in \mathcal{D}^{ad} \times \mathcal{O}^{ad} \times \mathcal{F}^{ad} \times \mathcal{C}^{ad}$ such that, given the initial conditions, $\forall\ (\delta\dot{\boldsymbol{d}}, \delta\dot{\boldsymbol{\theta}}) \in \dot{\mathcal{D}}^{ad,0} \times \dot{\mathcal{O}}^{ad,0}$:

$$\sum_{i=1}^{n_p} \boldsymbol{f}^{ext}_{/i} \cdot \delta\dot{\boldsymbol{d}}_i + \sum_{i=1}^{n_p} \boldsymbol{f}^{int}_{/i} \cdot \delta\dot{\boldsymbol{d}}_i + \sum_{i=1}^{n_p} \boldsymbol{c}^{ext}_{/i} \cdot \delta\dot{\boldsymbol{\theta}}_i + \sum_{i=1}^{n_p} \boldsymbol{c}^{int}_{/i} \cdot \delta\dot{\boldsymbol{\theta}}_i = \sum_{i=1}^{n_p} m_i\ddot{\boldsymbol{d}}_i \cdot \delta\dot{\boldsymbol{d}}_i + \sum_{i=1}^{n_p} I_i\ddot{\boldsymbol{\theta}}_i \cdot \delta\dot{\boldsymbol{\theta}}_i \qquad (5)$$

with:
$\mathcal{D}^{ad} = \{\boldsymbol{d} = \boldsymbol{d}_i(t)\ i = [1..n_p]\ \forall t \in [0,T]\}$
$\mathcal{O}^{ad} = \{\boldsymbol{\theta} = \boldsymbol{\theta}_i(t)\ i = [1..n_p]\ \forall t \in [0,T]\}$
$\mathcal{F}^{ad} = \{\boldsymbol{f} = \boldsymbol{f}^{int}_{/i}(t)\ i = [1..n_p]\ \forall t \in [0,T]\}$
$\mathcal{C}^{ad} = \{\boldsymbol{c} = \boldsymbol{c}^{int}_{/i}(t)\ i = [1..n_p]\ \forall t \in [0,T]\}$
n_p: total number of DEM particles.

2.3. Coupling approach

As mentioned in the previous sections, the coupling approach used here is based on the Arlequin approach [6, 7, 8]. This approach consists of:

1. A superposition of mechanical states in the given subdomains Ω_C and Ω_d with an overlapping zone Ω_O (Fig. 1).
2. A weak coupling (based on the weak formulation):
   (a) Definition of the gluing zone Ω_G:
   In this study, the gluing zone Ω_G is the same as the overlapping zone Ω_O. Hereafter, the term "overlapping zone" will be used to design the overlapping zone or the gluing zone.
   (b) Mediator space $\mathcal{M}$:
   To ensure the correct dialogue between the models, the control quantities in the overlapping zone must be chosen carefully. Here, the velocity coupling, in a weak sense in Ω_O), is chosen. From an algorithmic point of view, the velocity coupling is easier than the displacement coupling (Remark2). The mediator space denoted by $\mathcal{M}$ is defined as the space of the velocities defined in Ω_O.

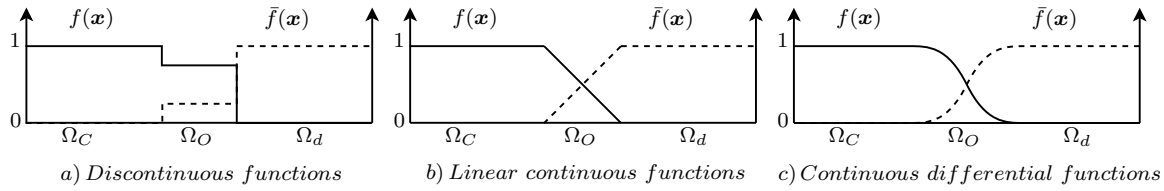

Figure 2: Examples of weight functions

(c) Projection operator and junction model:
The projection operator Π projects the continuum and discrete velocities on the mediator space. The junction model defines the linking conditions between the two models in the overlapping zone. To project the velocities on $\mathcal{M}$, an interpolation, whose shape functions will be defined later, is used. The junction model used in this work is the $H^1(\Omega_O)$ scalar product defined by:

$$< \boldsymbol{\lambda}, \boldsymbol{q} >_{H^1(\Omega_O)} = \int_{\Omega_O} \boldsymbol{\lambda} \cdot (\Pi \dot{\boldsymbol{u}} - \Pi \dot{\boldsymbol{d}}) + l^2 \boldsymbol{\varepsilon}(\boldsymbol{\lambda}) : \boldsymbol{\varepsilon}(\Pi \dot{\boldsymbol{u}} - \Pi \dot{\boldsymbol{d}})\, d\Omega \tag{6}$$

where $(\Pi \dot{\boldsymbol{u}} - \Pi \dot{\boldsymbol{d}})$ is the difference between the projected continuum and discrete velocities on Ω_O, $\boldsymbol{\lambda}$ is the Lagrange multiplier field and l, the junction parameter, is an H^1 coupling parameter.This parameter has the unit of a length, it is added to ensure the homogeneity of the integral terms of the H^1 coupling model. In this work, l is considered a variable parameter and will be studied in Section 3. If $l = 0$, the $H^1(\Omega_O)$ scalar product becomes equivalent to the $L^2(\Omega_O)$ scalar product (7) known as the Lagrange multiplier model.

$$< \boldsymbol{\lambda}, \boldsymbol{u} >_{L^2(\Omega_O)} = \int_{\Omega_O} \boldsymbol{\lambda} \cdot (\Pi \dot{\boldsymbol{u}} - \Pi \dot{\boldsymbol{d}})\, d\Omega \tag{7}$$

The displacement and velocity fields in Ω_C and Ω_d do not have the same nature. Indeed, Ω_C is a continuum whereas the Ω_d is a discrete subdomain. The discrete field associated with Ω_d is defined only at the particle positions. To be able to compute the junction models (6) and (7), an intepolation is defined on the DEM particles in Ω_O using shape functions, which will be defined later.

3. The energy partition between the continuum and discrete media in the overlapping zone:
As shown in Figure 1, the two models coexist in Ω_O. Therefore, the energies in this zone must be weighted, and, a kind of partition of unity in terms of energy is performed. Three weight functions, $\alpha(\boldsymbol{x})$, $\beta(\boldsymbol{x})$ and $\gamma(\boldsymbol{x})$, are introduced for the internal energy, the kinetic energy and the external work of the continuum subdomain, respectively. All of the functions verify the following:

$$\begin{array}{rccl} f(\boldsymbol{x}): & \Omega & \rightarrow & [0,1] \\ & \boldsymbol{x} & \rightarrow & \left\{ \begin{array}{ll} 1 & \text{in } \Omega_C \backslash \Omega_O \\ [0,1] & \text{in } \Omega_C \cap \Omega_O \\ 0 & \text{otherwise} \end{array} \right. \end{array} \tag{8}$$

In a complementary manner, the internal energy, the kinetic energy and the external work of the discrete subdomain are weighted by $\bar{\alpha}(\boldsymbol{x}) = 1 - \alpha(\boldsymbol{x})$, $\bar{\beta}(\boldsymbol{x}) = 1 - \beta(\boldsymbol{x})$ and $\bar{\gamma}(\boldsymbol{x}) = 1 - \gamma(\boldsymbol{x})$, respectively. Figure 2 presents examples of weight functions.

This coupling approach is applied to couple the continuum and the discrete models defined on Ω_C and Ω_d, respectively. By introducing the weight functions, in (2) and (5), and the coupling condition (6), the global weighted weak formulation becomes: find $(\boldsymbol{u}, \boldsymbol{d}, \boldsymbol{\theta}, \boldsymbol{\lambda}) \in \mathcal{U}^{ad} \times \mathcal{D}^{ad} \times \mathcal{O}^{ad} \times \mathcal{M}$ such that, given the initial conditions, $\forall\ (\delta\dot{\boldsymbol{u}}, \delta\dot{\boldsymbol{d}}, \delta\dot{\boldsymbol{\theta}}, \delta\dot{\boldsymbol{\lambda}}) \in \mathcal{U}^{ad,0} \times \mathcal{D}^{ad,0} \times \mathcal{O}^{ad,0} \times \mathcal{M}$:

$$
\begin{aligned}
&\int_{\Omega_C} \beta\, \rho\, \delta\dot{\boldsymbol{u}} \cdot \ddot{\boldsymbol{u}}\, d\Omega + \int_{\Omega_C} \alpha\, \boldsymbol{\varepsilon}(\delta\dot{\boldsymbol{u}}) : \boldsymbol{A} : \boldsymbol{\varepsilon}(\boldsymbol{u})\, d\Omega - \int_{\partial\Omega_C^T} \gamma\, \delta\dot{\boldsymbol{u}} \cdot \boldsymbol{T}_d\, d\Gamma - \int_{\Omega_C} \gamma\, \rho\, \delta\dot{\boldsymbol{u}} \cdot \boldsymbol{f}\, d\Omega \\
&+\sum_{i=1}^{n_p} \bar{\beta}_i\, m_i\, \ddot{\boldsymbol{d}}_i \cdot \delta\dot{\boldsymbol{d}}_i \; + \sum_{i=1}^{n_p} \bar{\beta}_i\, I_i\, \ddot{\boldsymbol{\theta}}_i \cdot \delta\dot{\boldsymbol{\theta}}_i \; - \sum_{i=1}^{n_p} (\bar{\gamma}_i\, \boldsymbol{f}_{/i}^{ext} + \bar{\alpha}_i\, \boldsymbol{f}_{/i}^{int}) \cdot \delta\dot{\boldsymbol{d}}_i \\
&-\sum_{i=1}^{n_p} (\bar{\gamma}_i\, \boldsymbol{c}_{/i}^{ext} + \bar{\alpha}_i\, \boldsymbol{c}_{/i}^{int}) \cdot \delta\dot{\boldsymbol{\theta}}_i \; + \delta \int_{\Omega_O} \boldsymbol{\lambda} \cdot (\Pi\dot{\boldsymbol{u}} - \Pi\dot{\boldsymbol{d}}) \; + \; l^2 \boldsymbol{\varepsilon}(\boldsymbol{\lambda}) : \boldsymbol{\varepsilon}(\Pi\dot{\boldsymbol{u}} - \Pi\dot{\boldsymbol{d}})\, d\Omega \qquad = \quad 0
\end{aligned}
\tag{9}
$$

2.4. Spatial discretization and integration issues

In the previous subsections, the global weak formulation (9) is presented in a continuous form. Now, the spatial discretization is introduced. In the literature, there are many interesting continuum methods used for solving partial differential equations, such as SPH [23], NEM [24] and FEM [25]. Each method is distinguished by its capability to spatially discretize the studied model. Among them, the constrained natural element method CNEM [26, 27, 28], which is an extension of the natural element method (NEM) [29] to non-convex domains, is chosen in this study. This method has practically all of the advantages of the FEM approach, and it circumvents the major drawbacks related to the meshing. Indeed, using the FEM approach, the approximation is dependent on the mesh quality. In contrast, using the CNEM approach, the approximation is dependent only on the relative position of the nodes [30]. Unlike the other mesh-free approaches: (i) the supports of constrained natural neighbor (CNN) shape functions used in CNEM approach are automatically defined, (ii) the values of CNN shape functions associated with internal nodes are null on the border of the domain. This last property is particularly interesting because it allows a direct imposition of the boundary conditions, exactly as in the finite elements framework. Given the broad similarity between the CNEM and FEM approaches, the CNEM-DEM coupling have the same performances as the FEM-DEM coupling with better applicability on complex domains and/or behaviors. Therefore, the continuum subdomain in Ω_C is discretized with the CNEM approach. Consequently, Ω_C is approximated by a set of nodes in which connectivity is not necessary [26].

To obtain a continuous field from the discrete quantities defined at the DEM particle positions in Ω_O, a constrained natural neighbor (CNN) interpolation is introduced in $\Omega_{d|\Omega_O}$. Thus, the particles associated with this subdomain are also considered CNEM nodes. The CNN interpolation is only applied in $\Omega_{d|\Omega_O}$, which is assumed to be far from the fine scale effects. The mediator space is also discretized with the CNEM approach. We denote by $\mathcal{M}_C^h$, $\mathcal{M}_d^h$ and $\mathcal{M}_O^h$ the discretized spaces of $\mathcal{U}^{ad}$, $\mathcal{D}^{ad}$ and $\mathcal{M}$, respectively. The associated discretized subdomains are designed Ω_C^h, Ω_d^h and Ω_O^h, respectively. The discrete domain Ω_d is a set of particles, then it is naturally discretized and $\Omega_d^h = \Omega_d$. According to the configurations of the discretized spaces in the overlapping zone, four cases can be distinguished (Fig. 3).
In this study and contrary to previous studies on continuum/discrete coupling approaches, no coincidence conditions are imposed on the coexisting discretized subdomains in Ω_O. Therefore, the fourth configuration is studied here (Fig. 3-d) as the general configuration that includes the three other configurations. This simplifies the use of this method in 3D complex domains. Indeed, in this case, it is sufficient to discretize the subdomains independently and mount them as indicated in Figure 3-d. In fact, using this configuration, it is very difficult to prove mathematically the existence and uniqueness of the solution. Also and contrary to the three other configurations, there are no numerical works, in literature, studying this configuration. Thus, the well posedness of the global problem will be analyzed numerically in this paper.

Using the CNN interpolation on the different discretized subdomains, Ω_C^h, Ω_O^h and $\Omega_{d|\Omega_O}^h$, the displacement fields $\boldsymbol{u}$ and $\boldsymbol{d}$ and the Lagrange multiplier unknowns $\boldsymbol{\lambda}$ are approximated by:

$$
\boldsymbol{u}^h(\boldsymbol{x}) = \sum_{i=1}^{n_C} N_i^C(\boldsymbol{x}) \boldsymbol{u}_i \tag{10}
$$

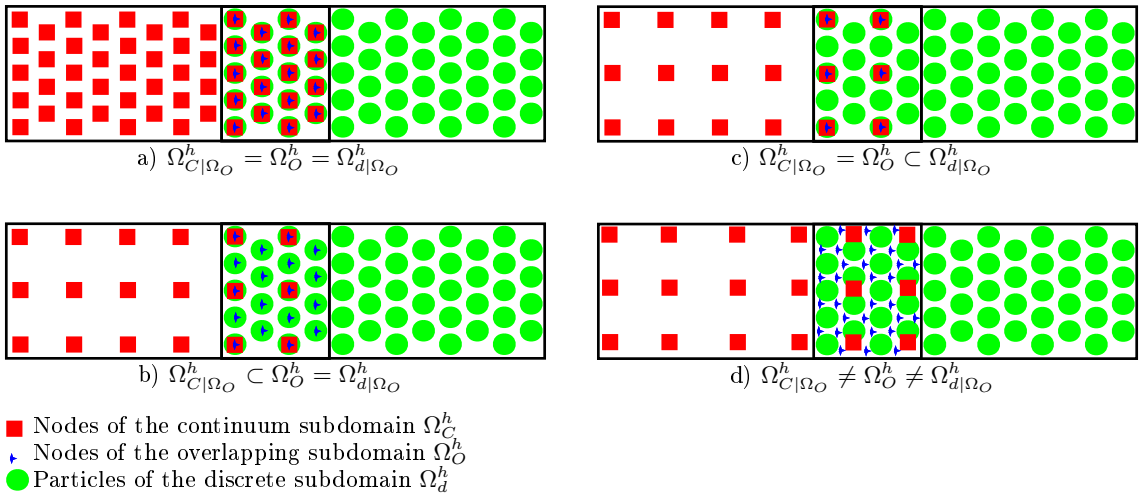

Figure 3: The different configurations of the discretized subdomains

$$\boldsymbol{d}^h(\boldsymbol{x}) = \sum_{i=1}^{n_{pO}} N_i^d(\boldsymbol{x})\boldsymbol{d}_i \tag{11}$$

$$\boldsymbol{\lambda}^h(\boldsymbol{x}) = \sum_{i=1}^{n_O} N_i^O(\boldsymbol{x})\boldsymbol{\lambda}_i \tag{12}$$

where n_C and n_O are total number of nodes located in Ω^h_C and Ω^h_O, respectively. n_{pO} is total number of particles located in $\Omega^h_{d|\Omega_O}$. $\boldsymbol{u}_i$ is the nodal displacements, $\boldsymbol{d}_i$ are the particle displacements and $\boldsymbol{\lambda}_i$ are the nodal Lagrange multipliers. N_i^C, N_i^O and N_i^d are the CNN shape functions constructed on Ω^h_C, Ω^h_O and $\Omega^h_{d|\Omega_O}$, respectively.

For the remainder of this paper, the superscript "h" will be omitted from the approximated quantities for clarity. Because the global weighted weak formulation (9) is true for any small arbitrary variations of $\dot{\boldsymbol{u}}$, $\dot{\boldsymbol{d}}$, $\dot{\boldsymbol{\theta}}$ and $\boldsymbol{\lambda}$, it can be reformulated as follows: find $(\boldsymbol{u}, \boldsymbol{d}, \boldsymbol{\theta}, \boldsymbol{\lambda}) \in \mathcal{U}^{ad} \times \mathcal{D}^{ad} \times \mathcal{O}^{ad} \times \mathcal{M}$ such that, given the initial conditions, $\forall\ (\delta\dot{\boldsymbol{u}}, \delta\dot{\boldsymbol{d}}, \delta\dot{\boldsymbol{\theta}}, \delta\dot{\boldsymbol{\lambda}}) \in \mathcal{U}^{ad,0} \times \mathcal{D}^{ad,0} \times \mathcal{O}^{ad,0} \times \mathcal{M}$:

$$\begin{aligned}&\int_{\Omega_C} \beta\, \rho\, \delta\dot{\boldsymbol{u}} \cdot \ddot{\boldsymbol{u}}\, d\Omega - \int_{\partial\Omega_C^T} \gamma\, \delta\dot{\boldsymbol{u}} \cdot \boldsymbol{T}\, d\Gamma + \int_{\Omega_C} \alpha\, \boldsymbol{\varepsilon}(\delta\dot{\boldsymbol{u}}) : \boldsymbol{A} : \boldsymbol{\varepsilon}(\boldsymbol{u})\, d\Omega - \int_{\Omega_C} \gamma\, \rho\, \delta\dot{\boldsymbol{u}} \cdot \boldsymbol{f}\, d\Omega \\ &+ \int_{\Omega_O} \boldsymbol{\lambda} \cdot \delta\Pi\dot{\boldsymbol{u}} + l^2 \boldsymbol{\varepsilon}(\boldsymbol{\lambda}) : \boldsymbol{\varepsilon}(\delta\Pi\dot{\boldsymbol{u}})\, d\Omega = 0\end{aligned} \tag{13}$$

$$\sum_{i=1}^{n_p} \bar{\beta}_i\, m_i\, \ddot{\boldsymbol{d}}_i \cdot \delta\dot{\boldsymbol{d}}_i \; - \sum_{i=1}^{n_p} (\bar{\gamma}_i\, \boldsymbol{f}^{ext}_{/i} + \bar{\alpha}_i\, \boldsymbol{f}^{int}_{/i}) \cdot \delta\dot{\boldsymbol{d}}_i - \int_{\Omega_c} \boldsymbol{\lambda}.\delta\Pi\dot{\boldsymbol{d}} + l^2 \boldsymbol{\varepsilon}(\boldsymbol{\lambda}) : \boldsymbol{\varepsilon}(\delta\Pi\dot{\boldsymbol{d}})\, d\Omega \;\; = \;\; 0 \tag{14}$$

$$\sum_{i=1}^{n_p} \bar{\beta}_i\, I_i\, \ddot{\boldsymbol{\theta}}_i \cdot \delta\dot{\boldsymbol{\theta}}_i - \sum_{i=1}^{n_p} (\bar{\gamma}_i\, \boldsymbol{c}^{ext}_{/i} + \bar{\alpha}_i\, \boldsymbol{c}^{int}_{/i}) \cdot \delta\dot{\boldsymbol{\theta}}_i = 0 \tag{15}$$

$$\int_{\Omega_O} \delta\boldsymbol{\lambda} \cdot (\Pi\dot{\boldsymbol{u}} - \Pi\dot{\boldsymbol{d}}) + l^2 \boldsymbol{\varepsilon}(\delta\boldsymbol{\lambda}) : \boldsymbol{\varepsilon}(\Pi\dot{\boldsymbol{u}} - \Pi\dot{\boldsymbol{d}})\, d\Omega \;\; = \;\; 0 \tag{16}$$

The integral terms will be computed numerically using an integration technique. Integration by a Gauss quadrature in the CNEM method adds considerable complexity to the solution procedure. The stabilized

conforming nodal integration [31, 32] presents a suitable alternative. This integration technique is used to compute the continuum terms using the Voronoï cells as the background of the integration. However, concerning the coupling terms, this technique cannot be applied directly. Indeed, the integrands include variables defined on different Voronoï diagrams. The issue here is how to choose the background of the integration. In this work, the Voronoï cells associated with the mediator space $\mathcal{M}_O^h$ are chosen as background of integration in the overlapping zone Ω_O. All of the variables that are not defined on $\mathcal{M}_O^h$ are projected on this space.
By replacing $\ddot{\boldsymbol{u}}$, $\delta\dot{\boldsymbol{u}}$, $\dot{\boldsymbol{d}}$, $\delta\dot{\boldsymbol{d}}$,$\boldsymbol{\lambda}$ and $\delta\boldsymbol{\lambda}$ by their approximated expressions in (13), (14), (15) and (16), the discretized equations can be written as:

- DEM equations:

$$\begin{array}{rcl} [m_\beta]\left\{\ddot{\boldsymbol{d}}\right\} & = & \left\{\boldsymbol{f}_\alpha^{int}\right\} + \left\{\boldsymbol{f}_\gamma^{ext}\right\} + \left\{\boldsymbol{f}^c\right\} \\ [I_\beta]\left\{\ddot{\boldsymbol{\theta}}\right\} & = & \left\{\boldsymbol{c}_\alpha^{int}\right\} + \left\{\boldsymbol{c}_\gamma^{ext}\right\} \end{array} \tag{17}$$

  where $(m_\beta)_{ij} = \bar{\beta}_i\,\delta_{ij}\cdot m_i$, $(I_\beta)_{ij} = \bar{\beta}_i\,\delta_{ij}\,I_i$, $(\boldsymbol{c}_\alpha^{int})_i = \bar{\alpha}_i\,\boldsymbol{c}_{/i}^{int}$, $(\boldsymbol{c}_\gamma^{ext})_i = \bar{\gamma}_i\,\boldsymbol{c}_{/i}^{ext}$, $(\boldsymbol{f}_\alpha^{int})_i = \bar{\alpha}_i\,\boldsymbol{f}_{/i}^{int}$, $(\boldsymbol{f}_\gamma^{ext})_i = \bar{\gamma}_i\,\boldsymbol{f}_{/i}^{ext}$ and $\{\boldsymbol{f}^c\} = [c_d]\,\{\boldsymbol{\lambda}\} = ([c_d^{L^2}] + l^2[c_d^{H^1}])\,\{\boldsymbol{\lambda}\}$ represents the total coupling force.

$$c_d^{L^2} \approx \sum_{K=1}^{n_O} V_I^O\,\left[N^d(\boldsymbol{x}_I)\right]^T\left[N^O(\boldsymbol{x}_I)\right]\,d\Omega \qquad \text{And} \qquad c_d^{H^1} \approx \sum_{K=1}^{n_O} V_I^O\,\left[\tilde{B}^d(\boldsymbol{x}_I)\right]^T\left[\tilde{B}^O(\boldsymbol{x}_I)\right]$$

  Where $\boldsymbol{x}_I$ are the coordinates of the I^{th} node of Ω_O^h, V_I^O is the volume of the Voronoï cell associated with I^{th} node of Ω_O^h, $\left[N^d\right]$ and $\left[N^O\right]$ are the interpolation matrices associated with Ω_d^h and Ω_O^h, respectively. $\left[\tilde{B}^d\right]$ and $\left[\tilde{B}^O\right]$ are the smoothed gradient matrices [31, 32] associated with Ω_d^h and Ω_O^h, respectively.

- CNEM equations

$$[M_\beta]\,\{\ddot{\boldsymbol{u}}\} = -\left\{\boldsymbol{F}_\alpha^{int}\right\} + \left\{\boldsymbol{F}_\gamma^{ext}\right\} - \left\{\boldsymbol{F}^c\right\} \tag{18}$$

  where $(M_\beta)_{ij} = \delta_{ij}\,\beta(\boldsymbol{x}_i)\,M_i$, M_i is the lumped mass of the i^{th} node located at $\boldsymbol{x}_i$ position, $\left\{\boldsymbol{F}_\alpha^{int}\right\} = [K_\alpha]\,\{\boldsymbol{u}\}$, $[K_\alpha]$ is the weighted stiffness matrix and $\{\boldsymbol{F}^c\} = [C_C]\,\{\boldsymbol{\lambda}\} = ([C_C^{L^2}] + l^2[C_C^{H^1}])\,\{\boldsymbol{\lambda}\}$ represents the total coupling force.

$$C_C^{L^2} \approx \sum_{K=1}^{n_O} V_I^O\,\left[N^C(\boldsymbol{x}_I)\right]^T\left[N^O(\boldsymbol{x}_I)\right]\,d\Omega \qquad \text{And} \qquad C_C^{H^1} \approx \sum_{K=1}^{n_O} V_I^O\,\left[\tilde{B}^C(\boldsymbol{x}_I)\right]^T\left[\tilde{B}^O(\boldsymbol{x}_I)\right]$$

  Where $\left[N^C\right]$ and $\left[\tilde{B}^C\right]$ are, respectively, the interpolation and smoothed gradient matrices associated with Ω_C^h.

- Interface equations: Equation 16 leads to:

$$[C_O]\,\{\ddot{\boldsymbol{u}}\} - [c_o]\left\{\dot{\boldsymbol{d}}\right\} = 0$$

  where: $[C_O] = \left[C_O^{L^2}\right] + l^2\left[C_O^{H^1}\right] = \left[C_C^{L^2}\right]^T + l^2\left[C_C^{H^1}\right]^T$ and $[c_o] = \left[c_o^{L^2}\right] + l^2\left[c_o^{H^1}\right] = \left[c_d^{L^2}\right]^T + l^2\left[c_d^{H^1}\right]^T$.

2.5. Time integration scheme and implementation

The numerical time integration is based on an explicit integration scheme that is well adapted for dynamic computations. Many explicit schemes can be used, such as the Runge-Kutta, position Verlet and velocity Verlet schemes. A comparison between these schemes can be found in [33]. According to this reference [33], the velocity Verlet scheme provides good results and is also easy to implement. For these reasons, this scheme is used in this paper to solve the global dynamic problem. This scheme gives an $O(h^3)$ approximation for both velocities and displacements. Thus, the velocity coupling, used in this work, does not affect the coupling approach accuracy compared to the displacement coupling.

2.5.1. DEM algorithm (DEM code)

- Initialization $\left\{\ddot{\boldsymbol{d}}\right\}_n$,$\left\{\dot{\boldsymbol{d}}\right\}_n$,$\{\boldsymbol{d}\}_n$,$\left\{\ddot{\boldsymbol{\theta}}\right\}_n$,$\left\{\dot{\boldsymbol{\theta}}\right\}_n$ and $\{\boldsymbol{\theta}\}_n$: The initial conditions or the interface results.
- Computation of $\{\boldsymbol{d}\}_{n+1}$ and $\{\boldsymbol{\theta}\}_{n+1}$:

$$\begin{aligned}\{\boldsymbol{d}\}_{n+1} &= \{\boldsymbol{d}\}_n + \Delta t\ \left\{\dot{\boldsymbol{d}}\right\}_n + \tfrac{\Delta t^2}{2}\ \left\{\ddot{\boldsymbol{d}}\right\}_n \\ \{\boldsymbol{\theta}\}_{n+1} &= \{\boldsymbol{\theta}\}_n + \Delta t\ \left\{\dot{\boldsymbol{\theta}}\right\}_n + \tfrac{\Delta t^2}{2}\ \left\{\ddot{\boldsymbol{\theta}}\right\}_n\end{aligned} \tag{19}$$

- Computation of $\left\{\boldsymbol{f}_\alpha^{int}\right\}_{n+1}$,$\left\{\boldsymbol{f}_\gamma^{ext}\right\}_{n+1}$, $\left\{\boldsymbol{c}_\alpha^{int}\right\}_{n+1}$et $\left\{\boldsymbol{c}_\gamma^{ext}\right\}_{n+1}$
- Computation of the predictive linear accelerations $\left\{\ddot{\boldsymbol{d}}\right\}_{n+1}^*$ (omitting the coupling forces $\{\boldsymbol{f}^c\}$ from Equation 17).

$$\left\{\ddot{\boldsymbol{d}}\right\}_{n+1}^* = [m_\beta]^{-1}\left(\left\{\boldsymbol{f}_\alpha^{int}\right\}_{n+1} + \left\{\boldsymbol{f}_\gamma^{ext}\right\}_{n+1}\right) \tag{20}$$

- Computation of the angular accelerations $\left\{\ddot{\boldsymbol{\theta}}\right\}_{n+1}$:

$$\left\{\ddot{\boldsymbol{\theta}}\right\}_{n+1} = [I_\beta]^{-1}\left(\left\{\boldsymbol{c}_\alpha^{int}\right\}_{n+1} + \left\{\boldsymbol{c}_\gamma^{ext}\right\}_{n+1}\right) \tag{21}$$

- Computation of the predictive linear velocities $\left\{\dot{\boldsymbol{d}}\right\}_{n+1}^*$:

$$\left\{\dot{\boldsymbol{d}}\right\}_{n+1}^* = \left\{\dot{\boldsymbol{d}}\right\}_n + \frac{\Delta t}{2}\left(\left\{\ddot{\boldsymbol{d}}\right\}_n + \left\{\ddot{\boldsymbol{d}}\right\}_{n+1}^*\right)$$

- Computation of the angular velocities $\left\{\dot{\boldsymbol{\theta}}\right\}_{n+1}$: $\left\{\dot{\boldsymbol{\theta}}\right\}_{n+1} = \left\{\dot{\boldsymbol{\theta}}\right\}_n + \frac{\Delta t}{2}\left(\left\{\ddot{\boldsymbol{\theta}}\right\}_n + \left\{\ddot{\boldsymbol{\theta}}\right\}_{n+1}\right)$
- Transfer of the predictive linear velocities and accelerations to the interface: $\left\{\dot{\boldsymbol{d}}\right\}_{n+1}^*$ and $\left\{\ddot{\boldsymbol{d}}\right\}_{n+1}^*$

2.5.2. CNEM algorithm (CNEM code)

- Initialization $\{\ddot{\boldsymbol{u}}\}_n$,$\left\{\dot{\boldsymbol{u}}\right\}_n$et $\{\boldsymbol{u}\}_n$: The initial conditions or the interface results.
- Computation of $\{\boldsymbol{u}\}_{n+1}$:

$$\{\boldsymbol{u}\}_{n+1} = \{\boldsymbol{u}\}_n + \Delta t\ \{\dot{\boldsymbol{u}}\}_n + \frac{\Delta t^2}{2}\ \{\ddot{\boldsymbol{u}}\}_n \tag{22}$$

- Computation of the predictive linear accelerations $\{\ddot{\boldsymbol{u}}\}_{n+1}^*$: (omitting the coupling forces $\{\boldsymbol{F}^c\}$ from Equation 18).

$$\{\ddot{\boldsymbol{u}}\}_{n+1}^* = [M_\beta]^{-1}\left(-\left\{\boldsymbol{F}_\alpha^{int}\right\}_{n+1} + \left\{\boldsymbol{F}_\gamma^{ext}\right\}_{n+1}\right) \tag{23}$$

- Computation of the predictive linear velocities $\left\{\dot{\boldsymbol{u}}\right\}_{n+1}^*$: $\left\{\dot{\boldsymbol{u}}\right\}_{n+1}^* = \left\{\dot{\boldsymbol{u}}\right\}_n + \frac{\Delta t}{2}\left(\{\ddot{\boldsymbol{u}}\}_n + \{\ddot{\boldsymbol{u}}\}_{n+1}^*\right)$
- Transfer of the predictive linear velocities and accelerations to the interface: $\left\{\dot{\boldsymbol{u}}\right\}_{n+1}^*$ and $\{\ddot{\boldsymbol{u}}\}_{n+1}^*$

2.5.3. Interface algorithm (Interface developed separately to couple the CNEM and DEM codes):

- Recovery of the predictive linear velocities from both the CNEM and DEM codes: $\{\dot{\boldsymbol{u}}\}^*_{n+1}$ and $\left\{\dot{\boldsymbol{d}}\right\}^*_{n+1}$
- Computation of $\{\boldsymbol{\lambda}\}_{n+1}$

$$\begin{array}{rcl} \{\dot{\boldsymbol{u}}\}_{n+1} & = & \{\dot{\boldsymbol{u}}\}^*_{n+1} - \frac{\Delta t}{2}\,[M_\beta]^{-1}\,\{\boldsymbol{F}^c\}_{n+1} \\ \left\{\dot{\boldsymbol{d}}\right\}_{n+1} & = & \left\{\dot{\boldsymbol{d}}\right\}^*_{n} + \frac{\Delta t}{2}\,[m_\beta]^{-1}\,\{\boldsymbol{f}^c\}_{n+1} \end{array} \tag{24}$$

$$\begin{array}{rcl} \{\boldsymbol{F}^c\}_{n+1} & = & [C_C]\,\{\boldsymbol{\lambda}\}_{n+1} \\ \{\boldsymbol{f}^c\}_{n+1} & = & [c_d]\,\{\boldsymbol{\lambda}\}_{n+1} \end{array} \tag{25}$$

$$[C_O]\,\{\dot{\boldsymbol{u}}\}_{n+1} - [c_o]\left\{\dot{\boldsymbol{d}}\right\}_{n+1} = 0 \tag{26}$$

By introducing Equations 24 and 25 into Equation 26, the interface system of equations can be written as:

$$[A]\,\{\boldsymbol{\lambda}\}_{n+1} = \{\boldsymbol{b}\}_{n+1} \tag{27}$$

where the coupling matrix $[A]$ and $\{\boldsymbol{b}\}_{n+1}$ are defined, respectively, as:

$$[A] = \frac{\Delta t}{2}([C_O]\,[M_\beta]^{-1}\,[C_C] + [c_o]\,[m_\beta]^{-1}\,[c_d]) \tag{28}$$

$$\{\boldsymbol{b}\}_{n+1} = [C_O]\,\{\dot{\boldsymbol{u}}\}^*_{n+1} - [c_o]\left\{\dot{\boldsymbol{d}}\right\}^*_{n+1} \tag{29}$$

By solving Equation 27, $\{\boldsymbol{\lambda}\}_{n+1}$ can be obtained.

- Computation of $\{\boldsymbol{F}^c\}_{n+1}$ and $\{\boldsymbol{f}^c\}_{n+1}$ using Equation 25.
- Computation of the linear velocities $\{\dot{\boldsymbol{u}}\}_{n+1}$ and $\left\{\dot{\boldsymbol{d}}\right\}_{n+1}$using Equation 24.
- The linear acceleration corrections: $\{\ddot{\boldsymbol{u}}\}_{n+1}$ and $\left\{\ddot{\boldsymbol{d}}\right\}_{n+1}$:

$$\begin{array}{rcl} \{\ddot{\boldsymbol{u}}\}_{n+1} & = & \{\ddot{\boldsymbol{u}}\}^*_{n+1} - [M_\beta]^{-1}\,\{\boldsymbol{F}^c\}_{n+1} \\ \left\{\ddot{\boldsymbol{d}}\right\}_{n+1} & = & \left\{\ddot{\boldsymbol{d}}\right\}^*_{n+1} + [m_\beta]^{-1}\,\{\boldsymbol{f}^c\}_{n+1} \end{array} \tag{30}$$

- Transfer of $\{\ddot{\boldsymbol{u}}\}_{n+1}$ and $\{\dot{\boldsymbol{u}}\}_{n+1}$ to the CNEM process and $\left\{\ddot{\boldsymbol{d}}\right\}_{n+1}$ and $\left\{\dot{\boldsymbol{d}}\right\}_{n+1}$ the DEM process.

Remark1:. The system (27) is solved using the well-known LU decomposition method [34]. Concerning the system (28), since the mass matrices of both continuum and discrete models are diagonals, it is easy to derive their inverse matrices and compute the coupling matrix A.

Remark2:. From an algorithmic point of view, the velocity coupling used in this work is easier than the displacement coupling. This is because the displacement coupling requires, in addition to the predictive accelerations and velocities, the computation of the predictive displacements which must be sent to the Interface code for correction. Therefore, in the case of displacement coupling, additional steps are necessary to compute and correct the predictive displacements. Whereas, in the case of velocity coupling, the correct displacement are obtained directly ((19) and (22)), thereby reducing the computational cost.

Remark3:. No explicit coupling conditions are applied to correct the angular velocities and accelerations of the particles in the overlapping zone. These quantities are corrected implicitly. Indeed, the internal forces are computed accounting for particle displacements and rotations. These forces are later used to compute the new displacements which are corrected using the coupling condition (16).

Remark4:. To be able to compute the predictive accelerations (Eqs. 20, 21 and 23), the lumped mass matrices must be invertible. Thus, the weight functions β and $\bar{\beta}$ must be strictly positive in Ω_O and at the border $\partial\Omega_O$. Then, a small ε will be used instead of zero at the nodes assigned to $\partial\Omega_O$. Therefore, the definition of this weight function β (8) is slightly modified as:

$$\begin{array}{rccl} \beta(\boldsymbol{x}): & \Omega & \rightarrow & [0,1] \\ & \boldsymbol{x} & \rightarrow & \left\{ \begin{array}{ll} 1 & \text{in } \Omega_C \backslash \Omega_O \\ [\varepsilon, 1-\varepsilon] & \text{in } \Omega_C \cap \Omega_O \\ 0 & \text{otherwise} \end{array} \right. \end{array} \tag{31}$$

where ε is a small strictly positive real number to be chosen.

2.5.4. Implementation

The DEM calculus is achieved using the GranOO workbench (Granular Object Oriented). Granoo was developed at the Mechanics institute of Bordeaux (I2M) by J.L. Charles et al. The code provides C++ libraries that implement classes useful to describe and solve dynamic mechanical problems using DEM and explicit temporal integration schemes. The CNEM calculus is achieved using a CNEM-based code, which was developed at the PIMM laboratory by G. Coffignal et al. It provides C++ libraries that interface with Python modules. The coupling between DEM and CNEM, described in the previous sections, is performed by an «interface» written in the Python language. This interface communicates directly with the CNEM-based process using Python classes. The Inter Process Communication (IPC) tool is used to ensure a synchronized communication between the GranOO process and the interface process.

3. Parametric study of the coupling parameters

Several works have studied mathematically the Arlequin method for both continuum-continuum coupling [7, 19, 20] and continuum-discrete coupling [21]. The main results concerning the well-posedness of the coupling problem are recalled in this paper. The weight function α must be strictly positive in Ω_O. Without this condition the coercivity of the internal energy cannot be verified. Another significant result concerning the coupling junction models is that for the discretized problem, contrary to the H^1 coupling which yields a well-posed problem, the L^2 coupling model can lead to an ill-conditioned system of equations, especially in the case of very small mesh size. In this context, Bauman et al. [21] have studied another coupling model, the H^1 seminorm, in which the first term of the H^1 model is removed. This model leads to a well-posed problem, but it does not constrain enough the continuum and discrete displacements in the overlapping zone. Other works [22, 35, 21] have studied numerically the ingredients of the Arlequin method using $1D$ models. Guidault et al. [22, 35] noted that, for the L^2 coupling model, the weight function α must be continuous at the boundary of the gluing zone $\partial\Omega_O$. Indeed, the use of a discontinuous weight function can cause undesirable free conditions at $\partial\Omega_O$.

Concerning the choice of the mediator space, Ben Dhia [7, 20] mentioned that in the case of continuous domains, it is convenient to choose $\mathcal{M} = \mathcal{H}^1(\Omega_O)$; however, it is very difficult to choose the finite approximation space $\mathcal{M}_O^h$. To address this difficulty, several works [22, 35, 21] proposed a 1D numerical study of $\mathcal{M}_O^h$. The different configurations that were studied are presented in a, b and c of Figure 3. The static studies of Guidault et al. [22] show that: (i) in the case of a fine multiplier space (Fig. 3-b), the response of the structure do not depend on the weight functions and a locking phenomenon takes place, i.e, the fine solution exactly conforms to the coarse solution in the overlapping zone; (ii) in the case of a coarse

Young's Modulus	Poisson's ratio	Radius ratio
$E_\mu = 265\ GPa$	$\nu_\mu = 0.3$	$\tilde{r}_\mu = 0.71$

Table 1: The micro properties of the cohesive beam bonds in the DEM subdomain
$\tilde{r}_\mu$ is an adimensional cohesive beam radius, defined as the ratio between the beam radius and the mean particle radius; E_μ and ν_μ are the micro Young modulus and the Poisson ratio of the beams, respectively.

multiplier space, the weight functions has an influence on the solutions such that the larger the weight function on the fine mesh, the smaller becomes the maximum jump between the two meshes.
This work proposes a 3D numerical dynamic study using the general configuration given in Figure 3-d. It will be demonstrated that some of the results proven in static using 1D models are not valid in 3D dynamic simulations.
Assuming the general case of the approximated Lagrange multiplier space, the various coupling parameters studied are:

- The junction model parameter l,
- The weight functions α, β and γ,
- The width of the overlapping domain L_O,
- The discretization of the approximated Lagrange multipliers space $\mathcal{M}_O^h$.

A 3D beam model is used for the dynamic study (Fig. 4), in which the length and the diameter are $L = 20\,mm$ and $D = 2\,mm$, respectively. The model is divided into two subdomains with an overlapping zone. The left subdomain is modeled by the CNEM approach using 626 nodes (the associated characteristic length is about $l_c = 0.47\,mm$) and fixed at the left end ($x = 0$). The right subdomain is modeled by the DEM approach using 20 000 spherical particles having $r_c = 0.05\,mm$ as mean radius. Based on the characteristic length of DEM and CNEM discretization (l_c and r_c), the cutoff frequencies of the two models can be determined: $f_c^{CNEM} = 1.9\,MHz$ and $f_c^{DEM} = 18.2\,MHz$. To control the high frequency wave reflexion at the CNEM-DEM interface, the free end ($x = L$) is submitted to a tensile loading with a very steep slope (Fig. 5). As shown in lower viewgraph of Figure 5, the Fourier spectrum contains powerful high frequency waves (greater than f_c^{CNEM}). The material of the beam is the silica: Young's modulus $E = 72\,GPa$, Poisson's ratio $\nu = 0.17$ and density $\rho = 2200\,Kg/m^3$. The corresponding micro properties of the cohesive beam bonds in the DEM approach are given in [1] and presented in Table 1.
To control the wave propagation in the model, four check points are placed along this beam (Fig. 4) as follows:

- CnemCheckPoint: at the middle of the CNEM subdomain where the controlled quantities are computed using the CNEM nodes in this zone
- OverlapCnemCheckPoint: at the middle of the overlapping zone where the controlled quantities are computed using only the CNEM nodes in this zone.
- OverlapDemCheckPoint: at the middle of the overlapping zone where the controlled quantities are computed using only the DEM particles in this zone.
- DemCheckPoint: at the middle of the DEM subdomain where the controlled quantities are computed using the DEM particles in this zone.

Figure 6 presents the reference results obtained by DEM and CNEM separately. Table 2 presents the mean displacement of the right end and the first three natural frequencies. It can be seen that the results are in good agreement, and they are also in agreement with the beam theory results. This ensures the equivalence of the two models.

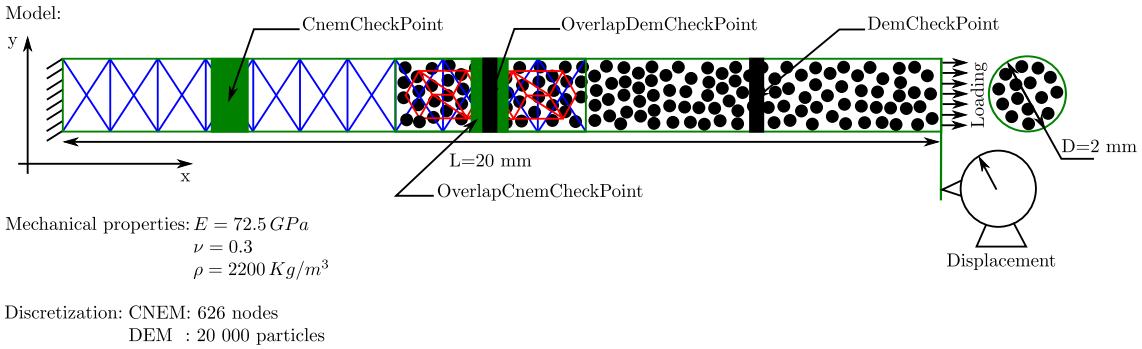

Figure 4: Beam model of the parameter studies

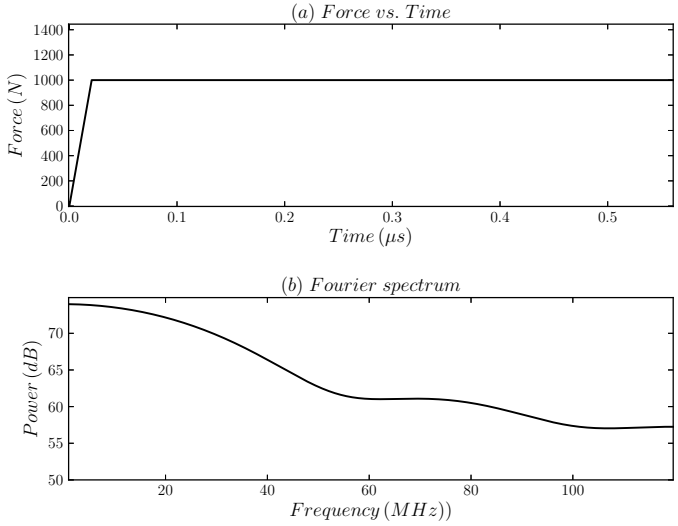

Figure 5: Tensile loading of study model and the associeted spectral analysis (computed from FFT)

	U_{mean} (mm)	f_0 (Hz)	f_1 (Hz)	f_2 (Hz)
Theory	0.087	71 757	215 272	358 787
DEM	0.083	72 408	217 246	362 072
CNEM	0.088	71 359	214 023	356 491

Table 2: Comparison of DEM, CNEM and analytical results

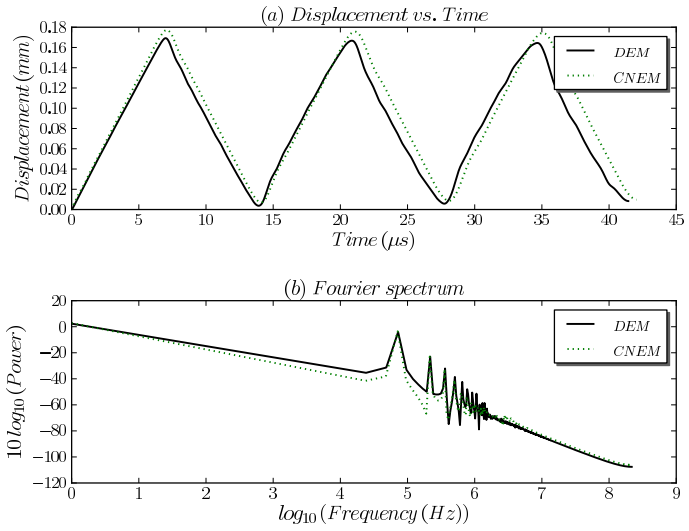

Figure 6: The free-end displacements obtained using DEM and CNEM separately and the associated spectral analyses (computed from FFT)

Remark5:. In this study, for the sake of simplicity, the weight functions are chosen as follows: $\alpha = \beta = \gamma$.

3.1. Influence of the junction parameter l

The parameter l is mainly employed to compute the coupling matrix A (28). The parameter's influence on the conditioning of A ($Cond = \|A\|.\|A^{-1}\|$) is analyzed. Figure 7 shows the conditioning of A with respect to l obtained for $L_O = 6\ mm$ using a coarse multiplier space and continuous weight functions with $\varepsilon = 0.005$ (ε is defined in (31)). The conditioning decreases with l and reaches a minimum at a small $l = l_{opt}$. Beyond this value, the conditioning increases exponentially as l increases. This is true for any choices of L_O, the weight functions and $\mathcal{M}_O^h$. Because l decreases the conditioning, H^1 coupling (6) for a small value of l, is better than L^2 coupling (7). However, contrary to what is presented in the literature, H^1 coupling becomes worse if l exceeds some small value. In practice, this parameter can be chosen as the characteristic length of the overlapping zone discretization $l_c^{\Omega_O}$ ($l_{opt} \approx l_c^{\Omega_O}$).
In the remainder of this section we will use the H^1 coupling with $l = l_{opt}$.

3.2. Influence of the weight functions

In this subsection, a fine discretization of the approximated multiplier space $\mathcal{M}_O^h$ is chosen, i.e, at the same scale as $\mathcal{M}_d^h$. The width of the overlapping zone L_O is fixed at 2 mm.

3.2.1. Constant weight functions $\alpha_{CNEM} = \alpha_{DEM} = 0.5$

The mean displacement obtained with the coupling method is 0.081 mm. This is in agreement with the reference mean displacements (Tab. 2). However, the temporal curve (Fig. 8) presents several deviations with regard to the reference curves. Figure 9 presents the velocities in the different check points (Figure 4) for the first round trip of the wave propagation. It can be seen that the major part of the high frequency waves (HFW) are reflected without entering the overlapping zone. Indeed, the HFW initially captured in the "DemCheckPoint" did not appear in "OverlapDemCheckPoint" or "OverlapCnemCheckPoint". This explains the deviation in the temporal displacement each time the global wave crosses the overlapping zone. Thus, constant weight functions are not a good choice for dynamic simulations. Indeed, the projection mechanism, which occurs in Ω_O, cannot dampen the HFW, and an additional filtering is required. In contrast, the static studies of Guidault et al. [22] showed that constant weight functions can be used with H^1 coupling.

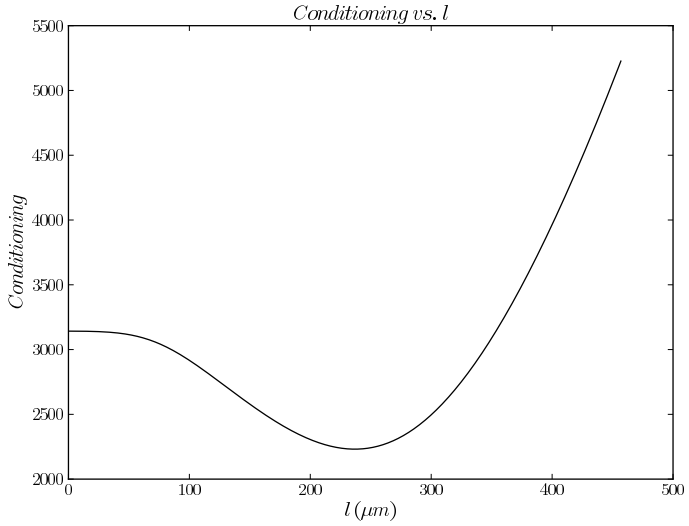

Figure 7: Conditioning of A with respect to l
$L_O = 6\,mm$, coarse Multiplier space, continuous weight functions with $\varepsilon = 0.005$

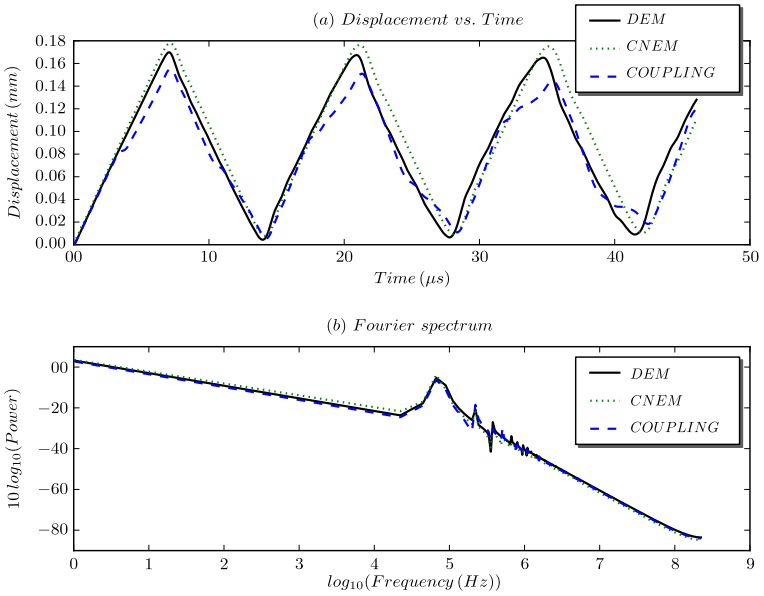

Figure 8: The free-end displacements obtained using DEM and CNEM separately and the coupling method, and the associated spectral analyses (computed from FFT)
$L_O = 2\,mm$, fine Multiplier space, constant weight functions $\alpha_{CNEM} = 0.5$

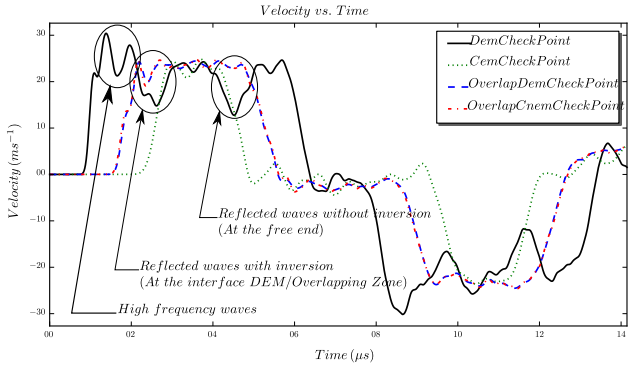

Figure 9: The linear velocities at the check points for the first round trip
$L_O = 2\,mm$, fine Multiplier space, constant weight functions $\alpha_{CNEM} = 0.5$

3.2.2. Constant weight functions $\alpha_{CNEM} \neq 0.5$

This sub-subsection analyzes the influence of the weight constant on the wave propagation. Two cases are studied here; the first case uses $\alpha_{CNEM} = 0.3$ (then, $\alpha_{DEM} = \bar{\alpha}_{CNEM} = 0.7$), and the second case uses $\alpha_{CNEM} = 0.8$ (then, $\alpha_{DEM} = 0.2$). The associated results are presented in Figure 10.

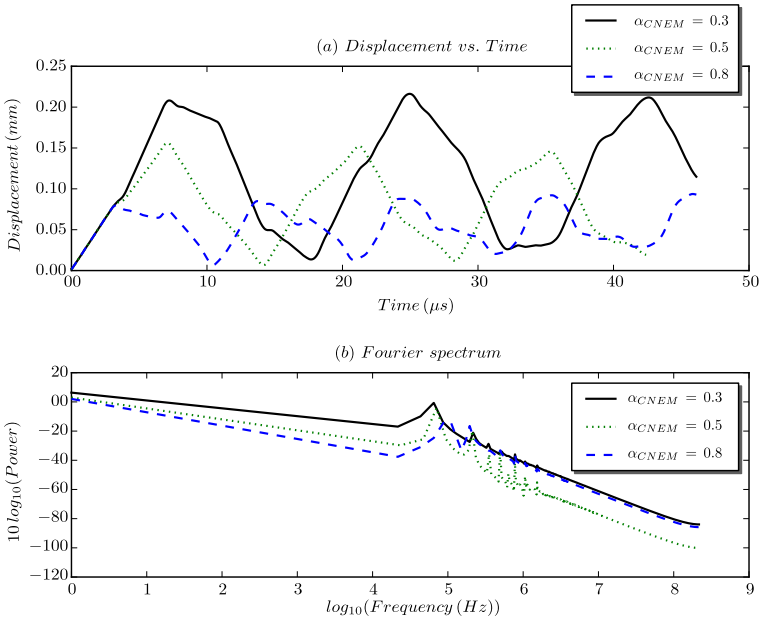

Figure 10: The free-end displacements obtained using DEM and CNEM separately and the coupling method, and the associated spectral analyses (computed from FFT) for different weight constants
$L_O = 2\,mm$, fine Multiplier space, constant weight functions $\alpha_{CNEM} = 0.3$, $\alpha_{CNEM} = 0.5$ and $\alpha_{CNEM} = 0.8$

A large difference between the results is observed. In the first case ($\alpha_{CNEM} = 0.3$), the magnitude of the free-end displacement is greater than that obtained using $\alpha_{CNEM} = 0.5$. However, it is smaller for the case of $\alpha_{CNEM} = 0.8$. To provide an explanation for these results, the temporal velocities at the check points are presented in Figure 11.
It can be seen that for $\alpha_{CNEM} = 0.8$, a portion of the principle wave is positively reflected at the interface between the two models, or more precisely, without entering the overlapping zone. Furthermore, only a complementary part is transmitted in the CNEM model. Quantitatively, the transmission and reflection

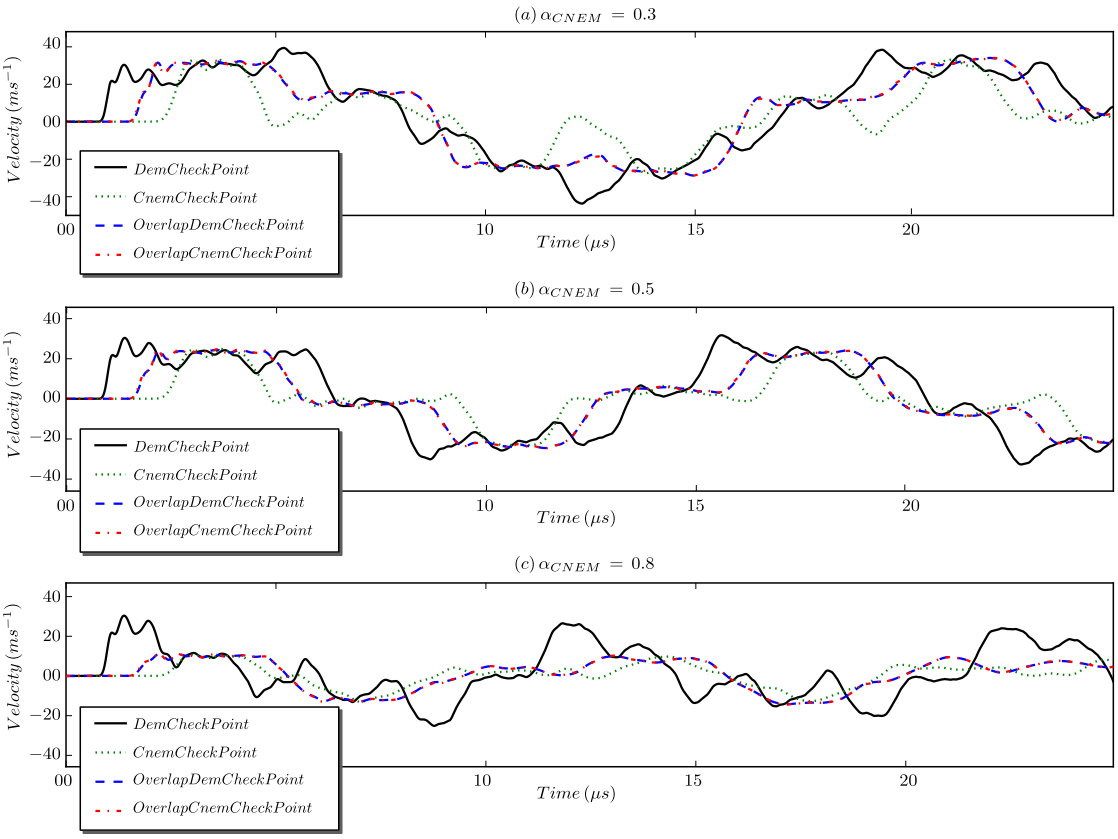

Figure 11: The linear velocities at the check points for different weight constants $L_O = 2\,mm$, fine Multiplier space, constant weighting $\alpha_{CNEM} = 0.3$, $\alpha_{CNEM} = 0.5$ and $\alpha_{CNEM} = 0.8$

coefficients can be introduced as:

$$t^{num}_{DEM-CNEM} = \frac{magnitude\ of\ the\ transmitted\ wave}{magnitude\ of\ the\ incident\ wave} = \frac{9{,}90}{22{,}01} = 0.44 \qquad \text{and} \qquad r^{num}_{DEM-CNEM} = 0.56$$

By analogy with the wave propagation between media with different acoustic impedances, the transmission and reflection coefficients can theoretically be defined as:

$$t^{th}_{DEM-CNEM} = \frac{2\ \alpha_{DEM}}{\alpha_{DEM}+\alpha_{CNEM}} \qquad \text{and} \qquad r^{th}_{DEM-CNEM} = \frac{\alpha_{CNEM}-\alpha_{DEM}}{\alpha_{DEM}+\alpha_{CNEM}}$$

Then, it can be verified that $t^{num}_{DEM-CNEM}$ and $r^{num}_{DEM-CNEM}$ are of the same order of magnitude as $t^{th}_{DEM-CNEM} = 0.4$ and $r^{th}_{DEM-CNEM} = 0.6$, respectively. For $\alpha_{CNEM} = 0.3$, the same reflection mechanism takes place but with a negative coefficient. Indeed, the velocity magnitude of the transmitted wave (measured at "CnemCheckPoint") is greater than the velocity magnitude of the forward wave (initially measured at "DemCheckPoint").

$$\left\{ \begin{array}{lcccl} t^{num}_{Dem-Cnem} & = & \frac{31.49}{21.86} & = & 1.44 \\ r^{num}_{Dem-Cnem} & = & 1-\frac{31.49}{21.86} & = & -0.44 \end{array} \right. \text{and} \left\{ \begin{array}{lcccl} t^{th}_{Dem-Cnem} & = & \frac{2\times 0.7}{1} & = & 1.4 \\ t^{num}_{Dem-Cnem} & = & 1-1.4 & = & -0.4 \end{array} \right.$$

Then, for the case of a constant weighting, $\alpha_{CNEM} = \alpha_{DEM} = 0.5$ must be used. Otherwise, there will be a reflection of a part of the principal forward wave. This result proves that the 1D static studies available in literature cannot be used to perform dynamic coupling. In effect, Guidault et al. [22] noted that, in statics and using a fine multiplier space, the solutions do not depend on the weight functions.

3.2.3. Continuous weight functions

As explained in Remark 4, the weight functions must not vanish at the boundary of the overlapping zone, and a small value ε must be adopted rather than 0 at $\partial\Omega_O$. Prior to studying the influence of the continuous weight functions, the influence of ε is studied. Figure 12 presents the free-end displacement using continuous weight functions for $\varepsilon = 0.05$, $\varepsilon = 0.005$ and $\varepsilon = 0.0005$ and the same conditions for L_O and $\mathcal{M}^h_O$. The parameter ε, when less than 0.05, has no practical influence on the results, but a very small ε can lead to instability problems. Indeed, as shown in Table 3, the smaller the ε, the greater the conditioning of the coupling matrix A becomes.

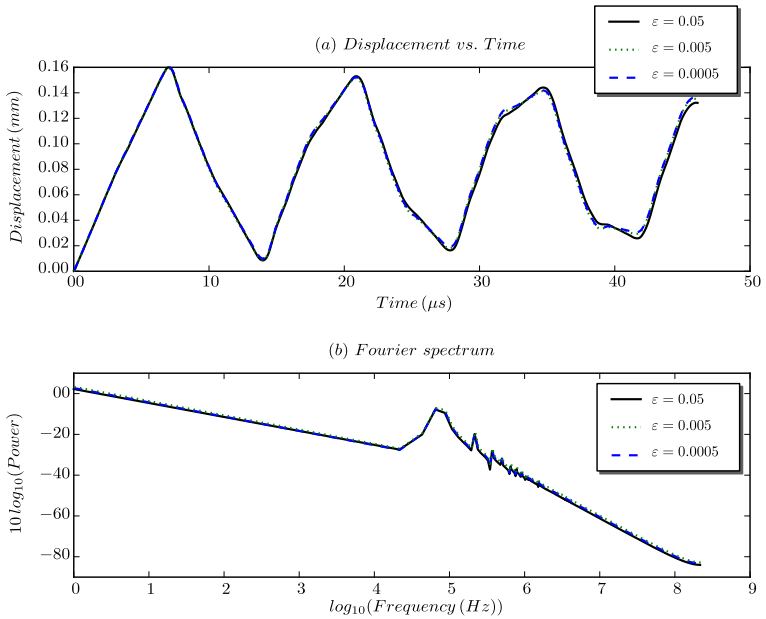

Figure 12: The free-end displacements obtained using the coupling method, and the associated spectral analyses (computed from FFT) for different values of ε

$L_O = 2\,mm$, fine Multiplier space, continuous weight functions

ε	0.05	0.005	0.0005
$Cond[A(l_{opt})]$	$2.53e4$	$8.93e4$	$5.67e5$

Table 3: Conditioning of A with respect to ε
$L_O = 2\,mm$, fine Multiplier space, continuous weight functions

In the remainder of this paper, $\varepsilon = 0.05$ will be chosen each time a continuous weight function is used. Figure 14 shows the free-end displacement for the case of a continuous weight function (Fig. 2-b). No high frequency waves (HFW) are reflected at the interface between the two models. Using continuous weight functions, the HFW enter the overlapping zone, and then, they are dampened by the projection onto the coarse space. The lower subplot in Figure 14 evidences that with a fine multiplier space, a small overlapping zone is sufficient to cancel out all of the HFW. As shown in Figure 13, the use of a continuous weight function significantly improves the results. However, a small deviation from the reference results still persists and becomes greater each time the wave travels back (CNEM-DEM direction). Because of the very fine discretization of the DEM subdomain, the weight of the particles in Ω_O decreases smoothly when approaching the CNEM subdomain. Therefore, the forward wave correctly crosses the interface between the pure DEM ($\Omega_d \backslash \Omega_O$) and the overlapping zone Ω_O. Thus, by examining the first round-trip (Fig. 13), it is apparent that no deviation from the references is noted when wave travels from the DEM subdomain to the CNEM subdomain. In the CNEM subdomain, a coarse discretization is used. The jump between the weights of two adjacent nodes is relatively large. The discrete weight functions of the CNEM subdomain are discontinuous staircase functions with large jumps. Thus, the same reflection mechanism, observed previously, occurs when the wave travels back (CNEM-DEM direction). To reduce the deviation, the width of the overlapping zone must be increased to reduce the slope of the weight functions. Another solution consists of using continuous differentiable weight functions (Fig. 2-c) to reduce the weighting jump in the vicinity of the overlapping zone boundary $\partial\Omega_O$. Figures 19, 20 and 21 present the results using the two solutions. The wave correctly crosses Ω_O without any deviation.

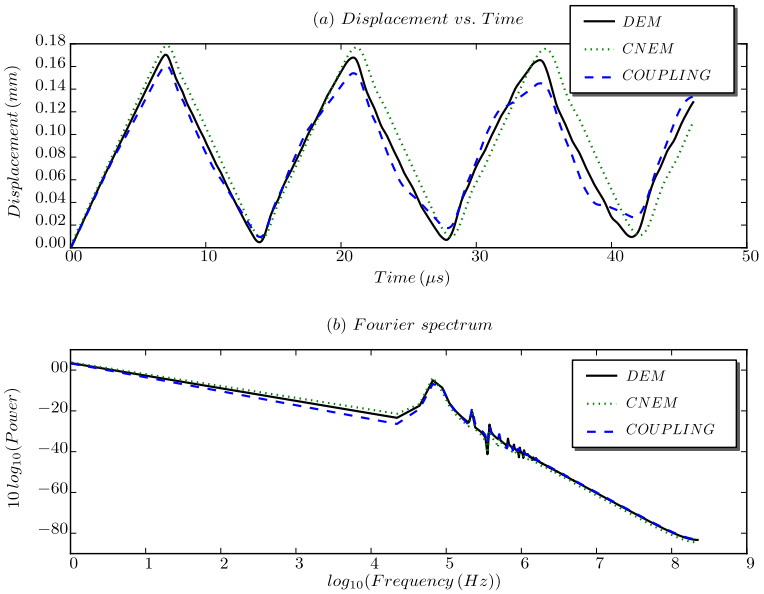

Figure 13: The free-end displacements obtained using DEM and CNEM separately and the coupling method, and the associated spectral analyses (computed from FFT)
$L_O = 2\,mm$, fine Multiplier space, continuous weight functions, $\varepsilon = 0.05$

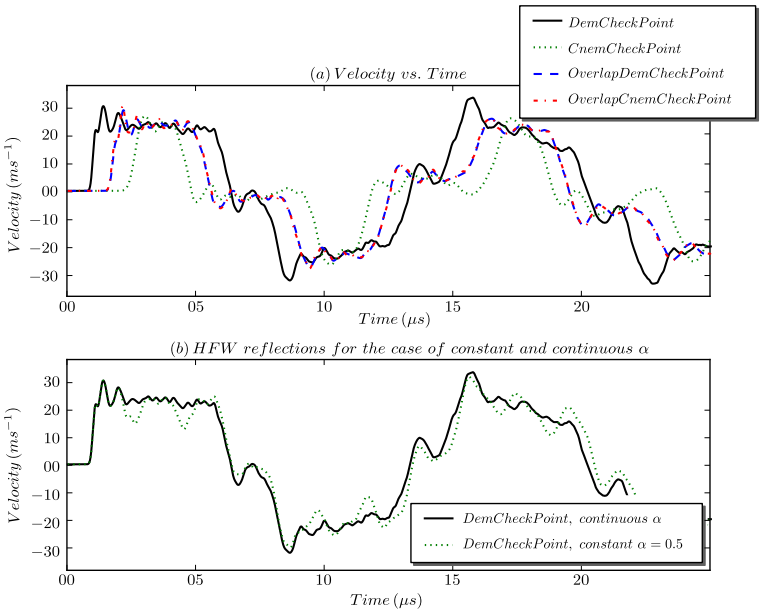

Figure 14: The linear velocities (a) at the different check points for the case of continuous α and (b) at the "DemCheckPoint" for the case of continuous and constant α

$L_O = 2\,mm$, fine Multiplier space, continuous weight functions, $\varepsilon = 0.05$

3.3. Influence of the approximated multiplier space $\mathcal{M}_O^h$

In the previous subsection, a fine multiplier space was used. In this case, the velocity in $\Omega_{d|\Omega_O}$ is practically locked at a value equal to the velocity in the $\Omega_{C|\Omega_O}$, as shown in the upper subplot of Figure 15. Indeed, the velocity curve at "OverlapDemCheckPoint" coincides with that at "OverlapCnemCheckPoint". The same locking phenomenon is noted when the second configuration (Fig. 3-b) is used [22]. Now, to study the influence of $\mathcal{M}_O^h$ on the results, a coarse multiplier space is used, i.e, at the same scale as $\mathcal{M}_C^h$. As shown in the bottom subplot of Figure 15, equality of the velocities in Ω_O is satisfied only in a weak sense and not in each multiplier space node. This allows the fine model (DEM model) to correctly act in Ω_O. However, in this case a small overlapping zone is insufficient to correctly transmit the principal tensile wave and cancel the high frequency waves.

3.4. Influence of the width of the overlapping zone L_O

It is apparent that for the case of fine multiplier space, the locking phenomenon occurs and a small L_O is sufficient to cancel the high frequency waves (HFW). Because the DEM particles are strongly constrained in Ω_O, the use of a large overlapping zone can slightly dampen the global free-end displacement (Fig. 16).

For the case of a coarse multiplier space, the DEM particles are able to correctly act in the overlapping zone. Then, even for the case of a large Ω_O, the global results will not be dampened. As shown in Figure 17, the larger the overlapping zone, the better the results become. Indeed, the use of a large Ω_O reduces the HFW reflection and allows a better transfer of the forward wave.

3.5. How to choose the coupling parameters in a general case?

In a general case, there is not an obvious method to determine, in a single way, the various coupling parameters to avoid wave reflexion. This subsection gives several recommendations and trends to choose correctly these parameters. The weight functions must be continuous. Indeed, with constant weight functions, the high frequency waves (HFW) are reflected without entering the overlapping zone and cannot be dampened by the projection mechanism. The choices of the width of the overlapping zone depends on the characteristic dimension of the discretization in this zone. In the case of fine discretization, a narrow overlapping zone is sufficient to dampen the HFW, because, the DEM particles are strongly constrained

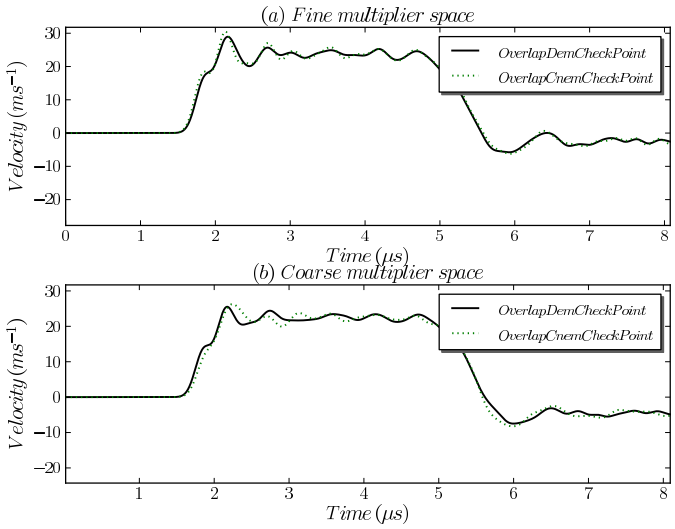

Figure 15: Velocity comparison in the overlapping zone using fine and coarse multipier spaces $L_O = 2\,mm$, continuous weight function, $\varepsilon = 0.05$

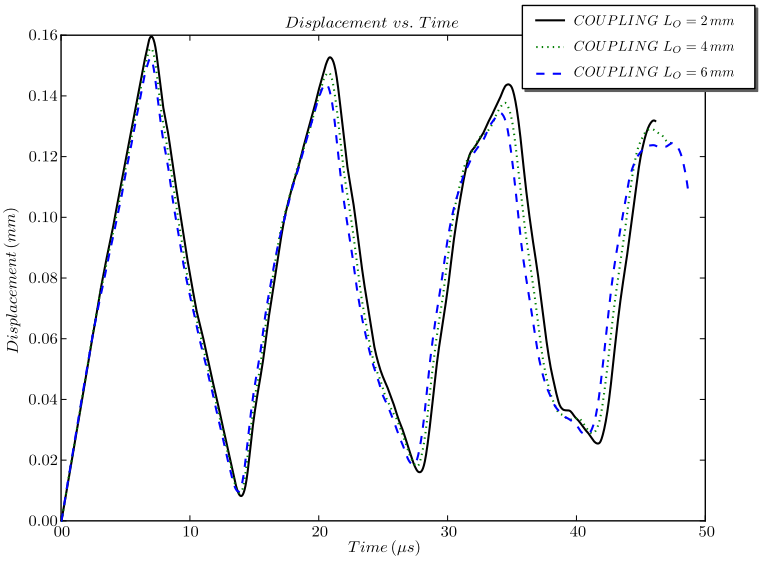

Figure 16: The free-end displacements obtained using the coupling method for $L_O = 2\,mm$, $L_O = 4\,mm$ and $L_O = 6\,mm$. Fine Multiplier space , continuous weight functions, $\varepsilon = 0.05$

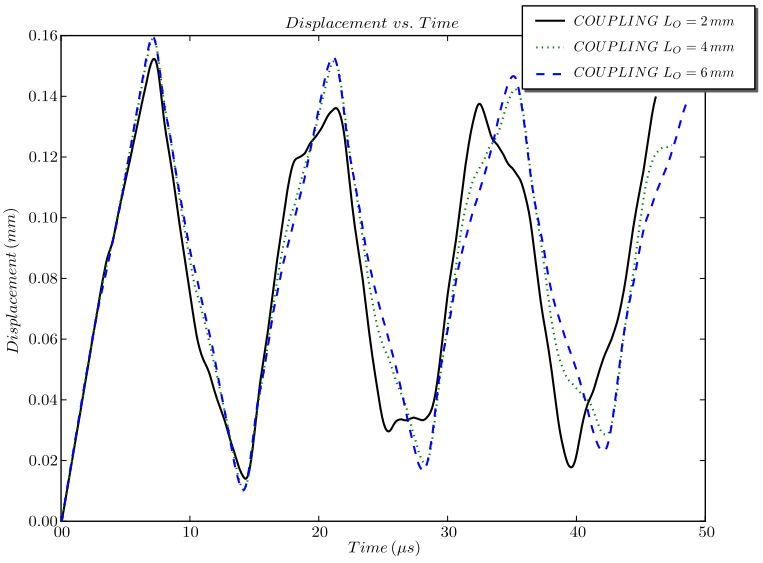

Figure 17: The free-end displacements obtained using the coupling method for $L_O = 2\,mm$, $L_O = 4\,mm$ and $L_O = 6\,mm$. Coarse Multiplier space , continuous weight functions, $\varepsilon = 0.05$

	Dynamic simulation
Coupling type	H^1 coupling
Junction parameter l	$l = l_{opt}$
Approximated Multiplier space	Coarse Multiplier space
Width of the overlapping zone L_O	As large as possible
Weight functions	Continuous , $\varepsilon = 0.05$

Table 4: Recommended Arlequin parameters for dynamic simulations

in Ω_O. On the contrary, coarse discretization requires a large Ω_O. To minimize the conditioning of the coupling matrix A, the H^1 coupling with $l = l_{opt}$ is recommended. l_{opt} can be chosen as the characteristic length of the overlapping zone discretization $l_c^{\Omega_O}$ ($l_{opt} \approx l_c^{\Omega_O}$). Table 4 presents the convenient Arlequin parameters to correctly perform the coupling.

4. Validation

The previous parametric-based study on tensile loading has allowed us to retain the convenient parameters to perform a correct coupling. In this section, the results of this study are used to validate the coupling between CNEM and DEM in a general 3D case. Contrary to the tensile case, in bending and torsion, the deformations in the cross sections are significant. To account for these effects, new geometric characteristics of the 3D model are used: $L = 100\,mm$ and $D = 20\,mm$ ($L/D = 5$). The DEM method is applied only for the portion located 20 mm from the right end (the section located at $x = L$) and the remainder of the model is modeled using the CNEM method (Fig. 18).
The following Arlequin's parameters are chosen: $L_O = 10\,mm$, continuous differentiable weight functions, $\varepsilon = 0.05$, $l = l_{opt}$ and coarse multiplier space.
Figures 19 and 20 present the temporal free-end displacements with respect to the x-axis and y-axis, respectively, using tensile and bending loading. The deviation from the reference, as observed in the previous simulations when the wave crosses the Ω_O, disappeared in the present results. Then, for this model, $L_O = 10$ mm is sufficient to correctly transmit the wave between the discrete and continuum models.

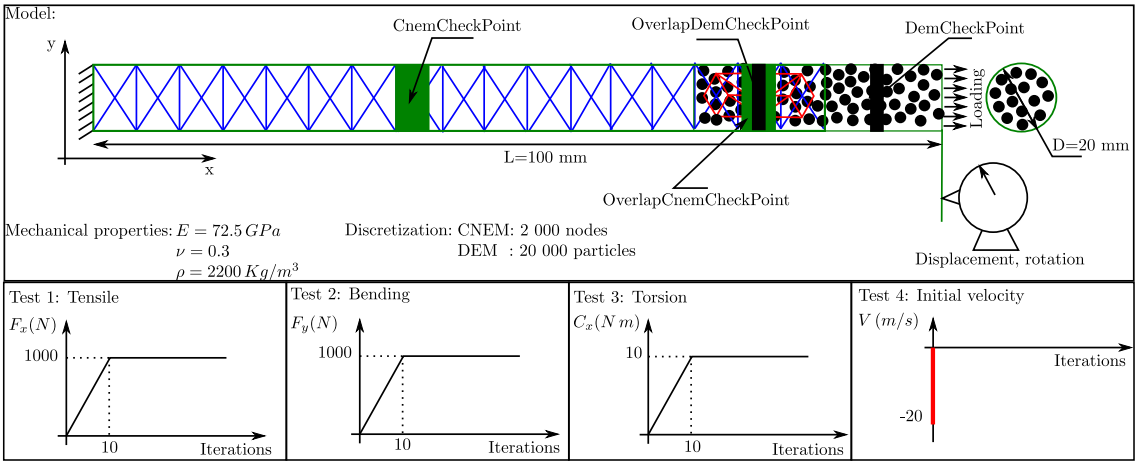

Figure 18: Validation model

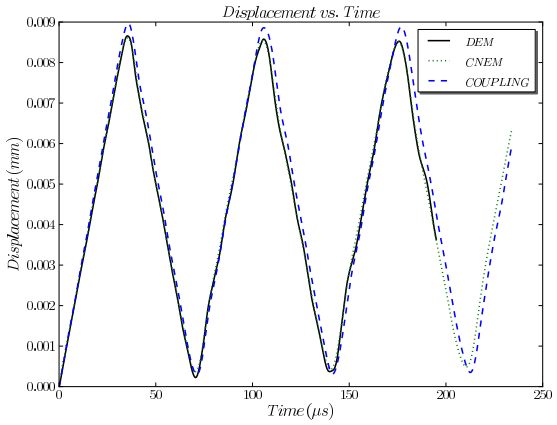

Figure 19: Test1: The free-end displacements $U_{x\ mean}$ obtained by DEM, CNEM and the coupling method $L_O = 10\,mm$, coarse Multiplier space , continuous differentiable weighting, $\varepsilon = 0.05$

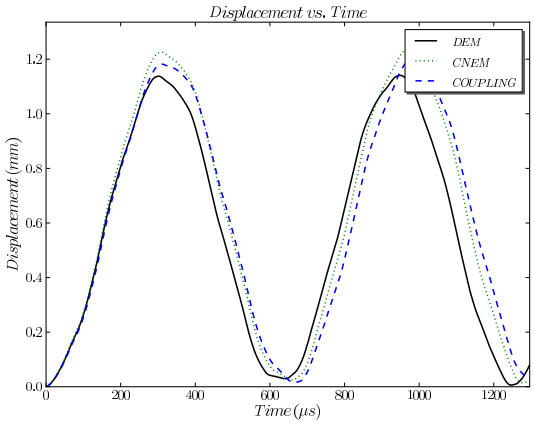

Figure 20: Test2: The free-end displacements $U_{y\ mean}$ obtained by DEM, CNEM and the coupling method $L_O = 10\,mm$, coarse Multiplier space , continuous differentiable weighting, $\varepsilon = 0.05$

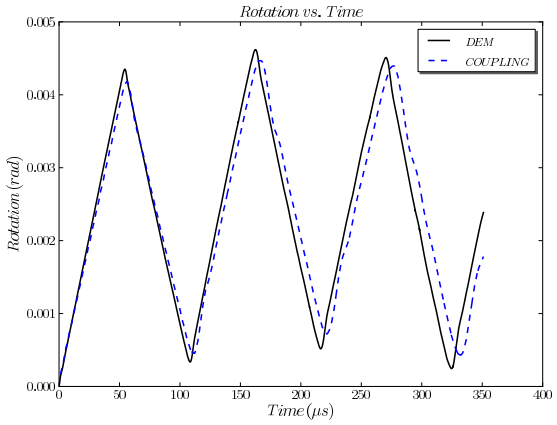

Figure 21: Test3: The free-end rotation $\theta_{x\ mean}$ obtained by DEM, CNEM and the coupling method $L_O = 10\,mm$, coarse Multiplier space , continuous differentiable weight functions, $\varepsilon = 0.05$

		Beam theory	DEM	CNEM	Coupling
Tensile	$U_{x\ mean}(mm)$	$4.40e-3$	$4.44e-03$	$4.49e-03$	$4.61e-03$
	$f_0(Hz)$	14 351	14 235	14 262	14 425
Bending	$U_{y\ mean}(mm)$	$5.85e-1$	$5.86e-1$	$6.27e-1$	$6.13e-1$
	$f_0(Hz)$	1 606	15 94	1 557	1 595

Table 5: Comparison of results
$L_O = 10\,mm$, coarse Multiplier space , continuous differentiable weight functions, $\varepsilon = 0.05$

Figure 21 presents the temporal free-end rotation about the x-axis using the torsional loading. The coupling results are in good agreement with the DEM results (Tab. 6).

Finally, the coupling method was tested using an initial velocity loading (Test 4 of Figure 18). Figure 22 presents the free-end displacement with respect to x-axis. The coupling result is comparable to the reference one.

The comparison (Figs. 19, 20, 22 and 21 and Tabs. 5 and 6) between the coupling results and the results obtained using DEM and CNEM separately, validates the new coupling method.

5. Conclusions

In this paper, based on the Arlequin approach, a 3D coupling method adapted for dynamic simulations is developed. This method couples two dissimilar methods: DEM-based method and CNEM-based method. Since the CNEM approach is a mesh-free method and has practically all the advantages of the FEM method, this coupling approach has the same performances as the FEM-DEM coupling with better applicability on complex problems.

At the beginning of this work, the Arlequin parameters are studied dynamically, using 3D models. The most general configuration is used in the overlapping zone (Fig. 3-d). As shown, the well posedness of the global problem is verified numerically. The H^1 coupling, for the case of a small junction parameter l_{opt},

		Beam theory	DEM	Coupling
Torsion	$\theta_{x\ mean}(mm)$	$2.05e-3$	$2.34e-3$	$2.32e-3$
	$f_0(Hz)$	9 382	9 252	9 106

Table 6: Comparison of results
$L_O = 10\,mm$, coarse Multiplier space , continuous differentiable weight functions, $\varepsilon = 0.05$

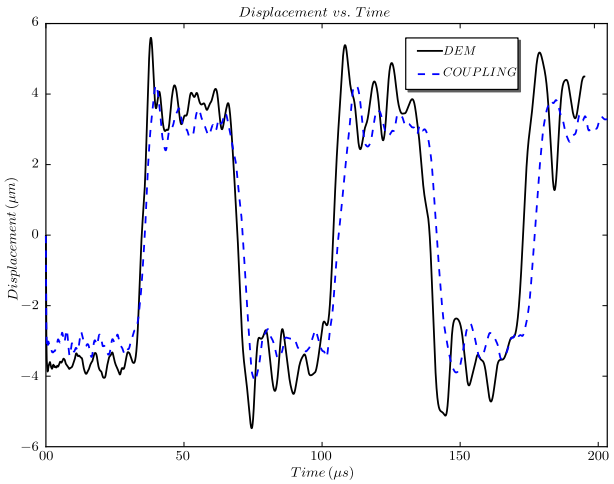

Figure 22: Test4: The free-end displacement $U_{x\ mean}$ obtained by DEM and the coupling method $L_O = 10\,mm$, coarse Multiplier space , continuous differentiable weight functions, $\varepsilon = 0.05$

is more accurate than the L^2 coupling. Indeed, it decreases the conditioning of the coupling matrix A. However, beyond l_{opt}, it can lead to instability problems or even divergence. Then, it is important to choose this parameter carefully. In the case of constant weight functions, $\alpha_{DEM} = \alpha_{CNEM} = 0.5$ must be chosen to ensure the correct transmission of the principal wave between the two models. Otherwise, a portion of the wave will be reflected in such a way that the reflection coefficient is proportional to $\alpha_{DEM} - \alpha_{CNEM}$. Additionally, with constant weight functions, the high frequency waves (HFW) are reflected without entering the overlapping zone, and, they cannot be dampened by the projection mechanism in Ω_O. Thus, continuous weight functions are better suited for dynamic simulations. This allows the HFW to enter the overlapping zone and be dampened by the projection mechanism. The results can be improved using continuous differentiable weight functions (Fig. 2-c). For the case of a fine multiplier space, the locking phenomenon takes place, and a narrow overlapping zone is sufficient to cancel the HFW. A large overlapping zone for the case of fine multiplier space can dampen the global wave, because the DEM particles in Ω_O are strongly constrained. In contrast, for the case of a coarse multiplier space, the larger the Ω_O, the better the results become. Indeed, large overlapping zone allows a better damping of the HFW. Additionally, because the particles in this zone can behave correctly (not strongly constrained), no damping of the global wave is noted.

[1] D. André, I. Iordanoff, J. Charles, J. Néauport, Discrete element method to simulate continuous material by using the cohesive beam model, Computer Methods in Applied Mechanics and Engineering 213-216 (2012) 113–125.

[2] I. Iordanoff, B. Seve, Y. Berthier, Solid Third Body Analysis Using a Discrete Approach: Influence of Adhesion and Particle Size on Macroscopic Properties, ASME Journal of tribology 124 (2002) 530–538. doi:10.1115/1.1456089.

[3] Z. Celep, Z. Bažant, Spurious reflection of elastic waves due to gradually changing finite element size, International journal for numerical methods in engineering 19 (1983) 631–646.

[4] T. Belytschko, S. Xiao, Coupling methods for continuum model with molecular model, International journal for Multiscale Computational Engineering 1 (1) (2003) 115–126.

[5] E. B. Tadmor, M. Ortiz, R. Phillips, Quasicontinuum analysis of defects in solids, Philosophical Magazine A 73 (6) (1996) 1529–1563.

[6] H. Ben Dhia, Problèmes mécanique multi-échelles: la méthode Arlequin, Comptes rendus de l 'académie des sciences - Analyse numérique (1998) 899–904.

[7] H. Ben Dhia, G. Rateau, Analyse mathématique de la méthode Arlequin mixte, Comptes rendus de l 'académie des sciences - Mécanique des solides et des stuctures (2001) 649–654.

[8] H. Ben Dhia, G. Rateau, The Arlequin method as a flexible engineering design tool, International journal for numerical methods in engineering 62 (2005) 1442–1462.

[9] F. Abraham, J. Broughton, N. Bernstein, E. Kaxiras, Spanning the continuum to quantum length scales in a dynamic simulation of brittle fracture, Europhysics Letters 44 (1998) 783–787.

[10] J. Broughton, F. Abraham, N. Bernstein, E. Kaxiras, Concurrent coupling of length scales: methodology and application, Physical review B 60 (4) (1999) 2391–2403.

[11] J. A. Smirnova, L. V. Zhigilei, B. J. Garrison, A combined molecular dynamics and finite element method technique applied to laser induced pressure wave propagation, Computer Physics Communications 118 (1999) 11–16.

[12] S. Xiao, T. Belytschko, A bridging domain method for coupling continua with molecular dynamics, Computer Methods in Applied Mechanics and Engineering.

[13] J. Fish, M. Nuggehally, M. Shephard, C. Picu, S. Badia, M. Parks, M. Gunzburger, Concurrent AtC coupling based on a blend of the continuum stress and the atomistic force, Computer Methods in Applied Mechanics and Engineering 196 (2007) 4548–4560.

[14] L. Chamoin, S. Prudhomme, H. Ben Dhia, J. T. Oden, Ghost forces and spurious effects in atomic-to-continuum coupling methods by the Arlequin approach, International journal for numerical methods in engineering 83 (2010) 1081–1113.

[15] P. Aubertin, J. Réthoré, R. De Borst, A coupled molecular dynamics and extended finite element method for dynamic crack propagation, International journal for numerical methods in engineering 81 (2010) 72–88.

[16] P. T. Bauman, J. T. Oden, S. Prudhomme, Adaptive multiscale modeling of polymeric materials with Arlequin coupling and Goals algorithms, Computer Methods in Applied Mechanics and Engineering 198 (5-8) (2009) 799–818.

[17] Y. Chuzel-Marmot, R. Ortiz, A. Combescure, Three dimentional SPH-FEM gluing for simulation of fast impacts on concrete slabs, Computers and Structures 89 (2011) 2484–2494.

[18] W. Curtin, R. Miller, Atomistic /continuum coupling in computational materials science, Modeling and simulation in matrerials science and engineering 11.

[19] G. Rateau, Méthode Arlequin pour les problèmes mécaniques multi-échelles Applications à des problèmes de jonction et de fissuration de structures élancées, Ph.D. thesis, École Centrale Paris (2003).

[20] H. Ben Dhia, Further Insights by Theoretical Investigations of the Multiscale Arlequin Method, International journal for Multiscale Computational Engineering 60 (3) (2008) 215–232.

[21] P. L. Bauman, H. Ben Dhia, N. Elkhodja, J. T. Oden, S. Prudhomme, On the application of the Arlequin Method to the Coupling of Particle and Continuum Models, Computational Mechanics 42 (2008) 511–530.

[22] P. Guidault, T. Belytschko, On the L2 and the H1 couplings for an overlapping domain decomposition method using Lagrange multipliers, International journal for numerical methods in engineering 70 (2007) 322–350.

[23] G. R. Liu, M. B. Liu, Smoothed particle hydrodynamics : a meshfree particle method, World Scientific Publishing Co. Pte. Ltd, 2003.

[24] N. Sukumar, B. Moran, T. Belytschko, The Natural Element Method in Solid Mechanics, International journal for numerical methods in engineering 43 (1998) 839–887.

[25] O. C. Zienkiewicz, R. L. Taylor, J. Z. Zhu, Finite Element Method: Its Basis & Fundamentals, Elsevier, 2005.

[26] F. Chinesta, E. Cueto, S. Cescotto, P. Lorong, Natural element method for the simulation of structures and processes, ISTE Ltd / John Wiley&Sons, 2011.

[27] J. Yvonnet, F. Chinesta, P. Lorong, D. Ryckelynck, The constrained natural element method (C-NEM) for treating thermal models involving moving interfaces, International Journal of Thermal Sciences 44 (2005) 559–569.

[28] J. Yvonnet, D. Ryckelynck, P. Lorong, F. Chinesta, A new extension of the natural element method for non-convex and discontinuous problems: the constrained natural element method (C-NEM), International journal for numerical methods in engineering 60 (2004) 1451–1474. doi:10.1002/nme.1016.

[29] N. Sukumar, B. Moranx, A. Y. Semenov, V. V. Belikovk, Natural neighbour Galerkin methods, International journal for numerical methods in engineering 50 (2001) 1–27.

[30] Illoul, P. Lorong, On some aspects of the CNEM implementation in 3D in order to simulate high speed machining or shearing, Computers and Structures, Computers and Structures 89 (2011) 940–958.

[31] J. Chen, C. Wu, S. Yoon, Y. You, A stabilized conforming nodal integration for Galerkin mesh-free methods, International journal for numerical methods in engineering 50 (2001) 435–466.

[32] D. González, E. Cueto, M. Martínez, M. Doblaré, Numerical integration in Natural Neighbour Galarkin methods, International journal for numerical methods in engineering 60 (2004) 2077–2114.

[33] E. Rougier, A. Munjiza, N. John, Numerical comparison of some explicit time integration schemes used in DEM, FEM/DEM and molecular dynamics, International journal for numerical methods in engineering 62 (2004) 856–879.

[34] A. Meyer, An efficient implementation of LU decomposition in C, Advances in Engineering Software 10 (3) (1988) 123–130.

[35] P. Guidault, T. Belytschko, Bridging domain methods for coupled atomistic-continuum models with L2 or H1 couplings, International journal for numerical methods in engineering 77 (2009) 1566–1592. doi:10.1002/nme.2461.